Engineering Fracture Mechanics 146 (2015) 185–209

Contents lists available at ScienceDirect

Engineering Fracture Mechanics

journal homepage: www.elsevier.com/locate/engfracmech

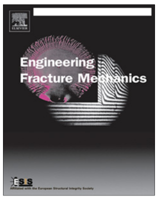

An engineering methodology for constraint corrections of elastic–plastic fracture toughness – Part II: Effects of specimen geometry and plastic strain on cleavage fracture predictions

Claudio Ruggieri [a,*], Rafael G. Savioli [a], Robert H. Dodds Jr. [b]

[a] Dept. of Naval Architecture and Ocean Engineering, University of São Paulo, São Paulo, Brazil
[b] Dept. of Civil and Environmental Engineering, University of Illinois at Urbana-Champaign, IL, USA

ARTICLE INFO

Article history:
Received 19 January 2015
Received in revised form 12 June 2015
Accepted 19 June 2015
Available online 4 August 2015

Keywords:
Cleavage fracture
Local approach
Weibull stress
Plastic strain
Probabilistic fracture mechanics

ABSTRACT

This work extends a micromechanics model for cleavage fracture incorporating effects of plastic strain to determine the reference temperature, T_0, for an A515 Gr 65 pressure vessel steel based on a modified Weibull stress $(\tilde{\sigma}_w)$. Non-linear finite element analyses for 3-D models of plane-sided SE(B) and PCVN specimens define the relationship between $\tilde{\sigma}_w$ and J from which the variation of fracture toughness across different crack configurations is predicted. The modified Weibull stress methodology yields estimates of T_0 from small fracture specimens which are in good agreement with the corresponding estimates derived from testing of larger crack configurations.

1. Introduction

The increasing demand to ensure acceptable levels of structural safety, including repair decisions and life-extension programs for aging structures, has spurred the development of advanced procedures for cleavage fracture assessments of critical engineering components such as, for example, nuclear reactor pressure vessels (RPVs), hydrocarbon-processing industry (HPI) pressurized equipment and storage tanks, among others. Current defect assessment procedures of large engineering structures [1–3] employ macroscopic measurements of cleavage fracture toughness (such as the J-integral at cleavage instability, J_c, or the critical Crack Tip Opening Displacement, CTOD or δ_c) derived from laboratory testing of conventional fracture specimens containing deep, through cracks $(a/W \geqslant 0.5)$. These toughness measures must satisfy parametric limits on the crack-tip deformation relative to crack length, specimen thickness and remaining crack ligament such that high constraint conditions, similar to those of small-scale yielding (SSY), are maintained over microstructurally significant size scales at the crack-tip region. However, much previous research shows the potentially strong effects of specimen geometry and loading mode on cleavage fracture toughness values $(J_c,\ \delta_c)$ measured over the low-to-mid range of the ductile-to-brittle transition (DBT) region for ferritic materials. When the toughness measuring capacity of the specimen is exceeded (as defined by $J_{max} = b\sigma_{ys}/M$ where M represents a nondimensional deformation limit, b denotes the uncracked ligament length and σ_{ys} defines the yield stress), the increased extension of plastic deformation prior to fracture affects the interaction between the global (remote) loading and boundary conditions with the local crack front fields (as determined uniquely by J) thereby

---

* Corresponding author. Tel.: +55 11 30915184; fax: +55 11 30915717.
E-mail address: claudio.ruggieri@usp.br (C. Ruggieri).

http://dx.doi.org/10.1016/j.engfracmech.2015.06.087
0013-7944/© 2015 Elsevier Ltd. All rights reserved.

Nomenclature

α	Weibull modulus (shape parameter) of toughness distribution
α_p	Weibull modulus (shape parameter) of particle distribution
$\bar{\epsilon}$	true (logarithmic) strain
$\bar{\sigma}$	true stress
β	power-law parameter of microcrack density function
δ	crack tip opening displacement
δ_c	critical value of crack tip opening displacement
ℓ	fractured particle size
ℓ_N	reference size of fractured particle
ϵ_p	effective plastic strain
ϵ_{ys}	material yield strain
η	nondimensional parameter describing the plastic contribution to the crack-tip strain energy
Γ	contour defined in a plane normal to the crack front
λ	average rate of fractured particles
ν	Poisson's ratio
Ω	volume of the fracture process zone
ψ	parameter defining the size of the fracture process zone
Ψ_c	fraction of fracture particles which become eligible to propagate unstably
ρ_0	initial crack tip blunting radius
σ_0	yield (reference) stress
σ_u	Weibull stress parameter
σ_w	Beremin Weibull stress
σ_1	maximum principal stress
σ_{ij}	Cartesian components of stress tensor
σ_{pf}	particle fracture stress
σ_{prs}	particle reference stress
σ_{uts}	material ultimate tensile strength
σ_{ys}	material yield stress
θ	polar coordinate
$\tilde{\sigma}_w$	modified Weibull stress
a	microcrack size, crack depth
a_0	initial crack size
B	specimen thickness
b	remaining crack ligament
b_0	initial size of remaining crack ligament
B_{eff}	effective specimen thickness
E	Young's modulus
E_d	particle's elastic modulus
J	J-integral
J_0	characteristic toughness of the Weibull distribution for J_c-values
J_2	second invariant of the stress deviator tensor
J_c	critical J-value (fracture toughness)
J_{avg}	average J-value over the crack front
J_{local}	J-value attained at a given point over the crack front
J_{max}	maximum J-value corresponding to a given deformation limit
J_{min}	threshold toughness of the 3-P Weibull distribution
K_0	characteristic toughness of the Weibull distribution for K_{Jc}-values
$K_{Jc-limit}$	maximum toughness value corresponding to a given deformation limit
K_{Jc-med}	median toughness of the Weibull distribution for K_{Jc}-values
K_{Jc}	critical value of the J-integral converted into K
K_{min}	threshold toughness of the 3-P Weibull distribution
m	Weibull modulus of Weibull stress distribution
N	total number of tested specimens
n	Ramberg–Osgood strain hardening exponent
n_j	outward normal to Γ
P_f	failure probability
Q	hydrostatic parameter quantifying the level of crack-tip constraint
R	residual function of the m-calibration procedure
r	polar coordinate

r_c	number of valid tests (uncensored data)
R_p	radius of the near-tip plastic region
S	specimen span
T	test temperature
T_0	reference temperature corresponding to a K_{Jc-med} of 100 MPa $\sqrt{\text{m}}$
u_i	Cartesian components of displacement
V	volume of material
V_0	reference volume
W	specimen width
W_s	stress-work density
X	Cartesian X-coordinate
Y	Cartesian Y-coordinate
Z	Cartesian Z-coordinate
1T	specimen thickness corresponding to 25 mm (1 in.)
$\bar{\mathbf{B}}$	strain–displacement matrix
API	American Petroleum Institute
C(T)	compact tension specimen
CMOD	crack mouth opening displacement
CTOD	crack tip opening displacement
CVE	Charpy V-notch energy
CVN	Charpy V-notch specimen
DBT	ductile-to-brittle transition
FPZ	fracture process zone
HPI	hydrocarbon-processing industry
LGC	large geometry change
MBL	modified boundary layer
PCVN	precracked Charpy specimen
RPV	reactor pressure vessel
SE(B)	single edge notch bend specimen
SSY	small scale yielding
TSM	toughness scaling model
WL	Wallin and Laukkanen particle distribution model

relaxing the levels of crack-tip constraint. Moreover, cleavage fracture is a very localized phenomenon with strong sensitivity to the random inhomogeneities at the microlevel of the material along the crack front and highly dependent on the local distribution of microcracks formed in the course of plastic deformation. Clearly, there is a rather complex coupling between the extension of plastic deformation prior to fracture and the statistical variability of local cleavage fracture resistance in the DBT region. These features greatly complicate the development of fracture mechanics procedures more applicable to cleavage fracture assessments.

A case of considerable interest is the utilization of small fracture specimens to facilitate experimental measurements of fracture toughness data in commercial nuclear RPV surveillance programs. In particular, three-point bend testing of precracked Charpy (PCVN) specimens becomes necessary when severe limitations exist on material availability such as, for example, in nuclear irradiation embrittlement studies. A recently developed procedure to characterize fracture toughness data over the DBT region, often known as the Master Curve approach [4–7] and standardized in the form of ASTM E1921 [8], makes extensive use in practice of PCVN specimens to determine a reference temperature, T_0, and the associated median fracture toughness applicable to a wide range of structural ferritic steels. The master curve methodology and ASTM E1921 represent a major advance in fracture testing programs with the incorporation of a statistical description for the scatter and specimen size effects on macroscopic fracture toughness values to define a normalized toughness dependence on temperature based on limited testing of relatively small specimens. However, as the specimen size is reduced (relative to the standard 1T specimen), the evolving crack-tip plastic zones developing from the free surfaces with increased loading affect strongly the crack front size over which high levels of near-tip stress triaxiality (constraint) are maintained. These changes in the crack-tip stress fields over a relatively small thickness in connection with a smaller sampling volume for cleavage fracture influence the measured toughness values, including their statistical scatter and mean value. Such features clearly affect the fracture toughness dependence on temperature and, consequently, produce potential differences in T_0-values measured using small size specimens and larger fracture specimens. While previous studies by Wallin et al. [9] and Joyce and Tregoning [10] suggest that use of subsized fracture specimens, including the PCVN configuration, provides acceptable, albeit slightly nonconservative, estimates of T_0, the issue of crack front constraint and its implications on small specimen toughness values continue to raise concerns in defect assessment and regulatory procedures.

In Part I of this work, Ruggieri and Dodds [11], hereafter referred to as R&D, described a micromechanics methodology based upon a local failure criterion incorporating the effects of plastic strain on cleavage fracture coupled with the statistics of microcracks. They considered a probabilistic framework to address the strong effects of constraint variations on (macroscopic) cleavage fracture toughness based on the Weibull stress concept (also widely known as the Beremin model [12]) but approached the modeling of cleavage fracture from the point of view of a coupling between the local plastic strain and the number of eligible Griffith-like microcracks nucleated from brittle particles dispersed into the ferrite matrix. A modified Weibull stress ($\tilde{\sigma}_w$) incorporating the effects of plastic strain on cleavage fracture emerged as a probabilistic fracture parameter to define conditions leading to (local) material failure. By postulating unstable crack propagation at a critical value of $\tilde{\sigma}_w$, a toughness scaling methodology that unifies toughness measures across different crack configurations and loading modes was introduced. Similar to the Beremin approach, the modified Weibull stress, $\tilde{\sigma}_w$, also follows a two-parameter Weibull distribution [13] defined by the Weibull modulus, m, and the scale parameter, σ_u. Further, the key parameter m also represents a material property [12,14,15] thereby providing the necessary framework to correlate fracture toughness for varying crack configurations under different loading conditions. Subsequent applications of the micromechanics methodology to assess effects of constraint in conventional fracture specimens showed that inclusion of plastic strain effects into the probabilistic framework to describe cleavage fracture reduces the amount of constraint correction from low-to-high constraint crack configurations, which is generally consistent with available toughness data.

However, despite the apparent promise of these fundamental studies, difficulties associated with the sensitivity of the micromechanics model to some specific features still remain, mostly connected with the calibration of the Weibull modulus defined by parameter m. Efforts in this area by Gao et al. [16], Ruggieri et al. [17], Gao and Dodds [18], Petti and Dodds [19,20] and Wasiluk et al. [21] advanced the understanding of the Weibull stress concept while, at the same time, evolving to characterize more adequately the effects of constraint variations on (macroscopic) cleavage fracture toughness. In particular, Gao et al. [16] and Ruggieri et al. [17] specifically introduced an improved calibration procedure for the Weibull modulus, m, based on fracture toughness data measured from two sets of test specimens exhibiting widely different levels of crack-tip constraint. While their calibration procedure has proven highly effective in producing unique m-values for applications of the standard Beremin model in fracture toughness predictions for common ferritic steels, it remains untested when different forms of the probabilistic fracture parameter, including the modified Weibull stress ($\tilde{\sigma}_w$) proposed earlier by R&D [11], are adopted. Since incorporation of plastic strain effects into the Weibull stress framework may plausibly exhibit different features than those associated with the conventional Beremin approach, additional analyses of the coupling effects between constraint variations and plastic strain directly connected to cleavage fracture predictions appear necessary.

This work describes a micromechanics methodology based upon a local failure criterion incorporating the often observed effects of plastic strain on cleavage fracture coupled with the statistics of microcracks. A central objective of this study is to explore application of the micromechanics model incorporating the influence of plastic strain on cleavage fracture developed in previous work by Ruggieri and Dodds [11] to correct fracture toughness for effects of constraint loss and, at the same time, to determine the reference temperature for pressure vessel steels from precracked Charpy (PCVN) specimens. Fracture toughness testing conducted on an A515 Gr 65 pressure vessel steel provides the cleavage fracture resistance data needed to assess specimen geometry effects on experimentally measured J_c-values. Very detailed non-linear finite element analyses for 3-D models of plane-sided SE(B) and PCVN specimens provide the evolution of near-tip stress field with increased macroscopic load (in terms of the J-integral) to define the relationship between $\tilde{\sigma}_w$ and J from which the variation of fracture toughness across different crack configurations is predicted. For the tested material, the modified Weibull stress methodology effectively removes the geometry dependence on J_c-values and yields estimates for the reference temperature, T_0, from small fracture specimens which are in good agreement with the corresponding estimates derived from testing of much larger crack configurations.

2. Local approach to cleavage fracture incorporating plastic strain effects

This section repeats the salient features of the Weibull stress framework incorporating plastic strain effects derived by R&D [11]. Development of a micromechanics model for cleavage fracture stress incorporating effects of plastic strain begins by assuming the near-tip fracture process zone (FPZ) in a stressed cracked body in which a small volume element, δV, is subjected to the principal stress, σ_1, and associated plastic strain, ϵ_p. Here, only microcracks formed from the cracking of brittle particles, such as carbides, in the course of plastic deformation contribute to cleavage fracture and the fraction of fractured particles increases with increased matrix plastic strain [22]. An approximate account of such a micromechanism can be made by considering that a fraction, Ψ_c, of the total number of brittle particles in the FPZ nucleates the microcracks which are eligible to propagate unstably and, further, that Ψ_c is a function of plastic strain but independent of microcrack size as described by R&D [11].

Following standard procedures based on the weakest link concept (see R&D [11]), a limiting distribution for the cleavage fracture stress can expressed as

$$P_f(\sigma_1,\ \epsilon_p) = 1 - \exp\left[-\frac{1}{V_0}\int_\Omega \Psi_c(\epsilon_p)\cdot\left(\frac{\sigma_1}{\sigma_u}\right)^m d\Omega\right] \tag{1}$$

where V_0 represents a reference volume conventionally taken as a unit volume and Ω is the volume of the near-tip fracture process zone most often defined as the loci where $\sigma_1 \geqslant \psi\sigma_0$, with σ_0 denoting the material yield stress and $\psi \approx 2$. The integral evaluated over Ω contains two contributions: one is from the principal stress criterion for cleavage fracture characterized in terms of σ_1 and the other is due the effective plastic strain, ϵ_p, which defines the number of eligible Griffith-like microcracks nucleated from the brittle particles effectively controlling cleavage fracture. The above result then motivates the notion of a modified Weibull stress, $\tilde{\sigma}_w$, defined by

$$\tilde{\sigma}_w = \left[\frac{1}{V_0}\int_\Omega \Psi_c(\epsilon_p)\cdot\sigma_1^m d\Omega\right]^{1/m}. \tag{2}$$

Clearly, when $\Psi_c = 1$, in which case all Griffith-like microcracks form immediately upon the onset of yielding, the above expression yields the standard Beremin model [12]. A number of possibilities exist to introduce treatments of plastic strain effects on cleavage fracture based on different suppositions about which specific feature controls cleavage microcracking or the unstable propagation of a fully formed Griffith-like microcrack. Here, we consider three cases of interest for defining the function Ψ_c which have a direct bearing on the connection between the Weibull stress and macroscale fracture toughness: (1) a local criterion incorporating the distribution of particle fracture stress [22,23]; (2) exponential dependence of eligible microcracks on ϵ_p [11] and (3) the influence of plastic strain on microcrack density [24,25]. As a further comparison, we also consider the modified form of the Weibull stress proposed by Beremin [12] as addressed next.

2.1. Local criterion using the distribution of particle fracture stress

To introduce a more detailed formulation for the cleavage failure probability, Wallin and Laukkanen (WL) [23], and earlier Wallin et al. [22], have argued that only a small number of all fractured particles actually contribute to the cleavage fracture process. Indeed, such an argument agrees with previous work of Hahn [26] who pointed out that only a fraction of the largest and most favorably oriented carbides participate in the cleavage microcracking process. Most importantly, though, the approach allows incorporation of plastic strain effects on the cleavage fracture probability through a particle fracture stress distribution developed by WL [23]. Following similar arguments as those given in their work, we can derive the failure probability of cleavage fracture including effects of plastic strain as follows: let Ψ_c now be the fraction of fractured particles defined by WL [23] as a two-parameter Weibull distribution in the form

$$\Psi_c = 1 - \exp\left[-\left(\frac{\ell}{\ell_N}\right)^3\cdot\left(\frac{\sigma_{pf}}{\sigma_{prs}}\right)^{\alpha_p}\right] \tag{3}$$

where ℓ is the particle size, ℓ_N represents a reference particle size, σ_{prs} is the particle reference fracture stress, α_p denotes the Weibull modulus and $\sigma_{pf} = \sqrt{1.3\sigma_1\epsilon_p E_d}$ characterizes the particle fracture stress in which σ_1 is the maximum principal stress, ϵ_p denotes the effective matrix plastic strain and E_d represents the particle's elastic modulus. The term $(\ell/\ell_N)^3$ appearing in the above expression simply reflects the weakest link character of the particle fracture stress distribution as Ψ_c decreases with increased particle sizes, ℓ (see WL [23] for additional details). For ferritic structural steels, such as the A515 pressure vessel material utilized in this study, typical values of α_p and E_d are often taken as 4 and 400 GPa [23]; these values are employed in the analyses reported later in Section 6.

Now, assuming that a fractured particle with size ℓ becomes a Griffith-like microcrack with the same size, the probability distribution for the fracture stress of a cracked solid with increased levels of loading yields

$$P_f(\sigma_1,\ \epsilon_p) = 1 - \exp\left[-\frac{1}{V_0}\int_\Omega\left\{1-\exp\left[-\left(\frac{\sigma_{pf}}{\sigma_{prs}}\right)^{\alpha_p}\right]\right\}\cdot\left(\frac{\sigma_1}{\sigma_u}\right)^m d\Omega\right] \tag{4}$$

from which the Weibull stress now takes the form

$$\tilde{\sigma}_w = \left[\frac{1}{V_0}\int_\Omega\left\{1-\exp\left[-\left(\frac{\sigma_{pf}}{\sigma_{prs}}\right)^{\alpha_p}\right]\right\}\cdot\sigma_1^m d\Omega\right]^{1/m} \tag{5}$$

where it is understood that the fraction of fractured particles defined by Eq. (3) is assumed independent of the particle size, ℓ, so that the ratio $\ell/\ell_N \to 1$ and, further, the particle reference stress, σ_{prs}, now represents an approximate average for the distribution of the particle fracture stress.

Here, it is of interest to note that the approximation $\ell/\ell_N \to 1$ was made to simplify the resulting failure probability that would otherwise be solvable only by numerical methods and, at the same time, to arrive at a closed form for the Weibull stress given by Eq. (5) – (R&D [11] discuss this simplification in detail). Moreover, rearranging the above two-parameter Weibull distribution for the particle fracture stress, the scale parameter of Eq. (3) can be rewritten as $\sigma_{prs}/(\ell_N/\ell)^{3/\alpha_p}$. Since the calibration procedure addressed later relies on determining the value of the average particle fracture stress that provides the best correction for cleavage fracture toughness data measured from two sets of test specimens with sufficiently differing constraint levels, use of σ_{prs} or $\sigma_{prs}/(\ell_N/\ell)^{3/\alpha_p}$ should scale the Weibull stress trajectories but with no significant impact on fracture toughness predictions. Consequently, it is simpler to fix $\ell/\ell_N = 1$ at the onset of the analysis and proceed with the calibration of σ_{prs} as addressed later in Section 6.

2.2. Exponential dependence of eligible microcracks on ϵ_p

Recent extensions of the Beremin model made by Bordet et al. [27] include plastic strain effects on cleavage fracture in terms of the probability for nucleating a carbide microcrack. Their original model considers that only freshly nucleated carbide microcracks, which become Griffith-like microflaws, are eligible to propagate unstably. Here, we take a viewpoint similar to that implied in the analysis of Bordet et al. [27] and adopt a Poisson distribution [13,28,29] with parameter λ to define Ψ_c given by

$$\Psi_c = 1 - \exp(-\lambda\epsilon_p) \tag{6}$$

where λ can be interpreted as the average rate of fractured particles that become Griffith-like microcracks with a small strain increment. Here, the underlying assumption is associated with a Poisson process [29] to describe the number of fractured particles that become eligible to propagate unstably thereby driving the cleavage fracture. Thus, the cleavage failure probability becomes

$$P_f(\sigma_1,\ \epsilon_p) = 1 - \exp\left\{-\frac{1}{V_0}\int_\Omega \left[1 - \exp(-\lambda\epsilon_p)\right]\cdot\left(\frac{\sigma_1}{\sigma_u}\right)^m d\Omega\right\} \tag{7}$$

from which the modified Weibull stress is written as

$$\tilde{\sigma}_w = \left\{\frac{1}{V_0}\int_\Omega \left[1 - \exp(-\lambda\epsilon_p)\right]\cdot\sigma_1^m d\Omega\right\}^{1/m}. \tag{8}$$

where the exponential character describing the first term of the integrand ensures that $\Psi_c \to 1$ for large values of ϵ_p, which is consistent with the condition that the fraction of microcracks which are eligible to propagate unstably increases with increased plastic strain. Further observe that similar behavior also holds for the particle distribution model and the associated modified Weibull stress expressed by previous Eq. (5).

2.3. Influence of plastic strain on microcrack density

Previous fundamental work [24,25] clearly shows the strong effect of plastic deformation, in the form of inhomogeneous arrays of dislocations, on microcrack nucleation which triggers cleavage fracture at the material microlevel. Based upon direct observations of cleavage microcracking by plastic strain made in ferritic steels at varying temperatures [30–32], the probability distribution for the fracture stress of a cracked solid with increased levels of loading yields

$$P_f(\sigma_1,\ \epsilon_p) = 1 - \exp\left[-\frac{1}{V_0}\int_\Omega \epsilon_p^\beta\cdot\left(\frac{\sigma_1}{\sigma_u}\right)^m d\Omega\right] \tag{9}$$

where it is understood that $\Psi_c(\epsilon_p) = \epsilon_p^\beta$. Thus, the modified Weibull stress becomes

$$\tilde{\sigma}_w = \left[\frac{1}{V_0}\int_\Omega \epsilon_p^\beta\cdot\sigma_1^m d\Omega\right]^{1/m}. \tag{10}$$

The above plastic term correction simply describes the increase in cleavage fracture probability that results from the growth in microcrack density with increased levels of near-tip plastic strain. As already discussed by R&D [11], this form of Ψ_c does not provide an exact description for the fraction of microcracks nucleated inside the near-tip fracture process zone with increased deformation which are eligible to propagate unstably. Similar approaches adopting the same viewpoint of a functional form between microcrack density and plastic strain include the works of Kroon and Faleskog [33], Gao et al. [34] and Ruggieri [35].

2.4. Modified Beremin model

The important role of plastic deformation on cleavage fracture has also been recognized in the early work of the Beremin group [12]. Based on experimental analyses of the failure strain for tensile notched specimens made of an ASTM A508 steel, they modified the previous Eq. (1) to define a modified form for the limiting distribution of the cleavage fracture stress as

$$P_f(\sigma_1,\ \epsilon_p) = 1 - \exp\left[-\frac{1}{V_0}\int_\Omega \exp\left(-\frac{m\epsilon_p}{2}\right)\cdot\left(\frac{\sigma_1}{\sigma_u}\right)^m d\Omega\right] \tag{11}$$

with the Weibull stress defined by

$$\tilde{\sigma}_w = \left[\frac{1}{V_0}\int_\Omega \exp\left(-\frac{m\epsilon_p}{2}\right)\cdot\sigma_1^m d\Omega\right]^{1/m} \tag{12}$$

which indicates that $\tilde{\sigma}_w$ varies approximately with $\exp(-\epsilon_p/2)$. Since $\Psi_c = \exp(-m\epsilon_p/2)$ in the above equation, observe the prominent role of the plastic strain at very low levels of ϵ_p (in which case $\Psi_c \to 1$) and a minimal effect for large values of ϵ_p such that $\Psi_c \to 0$.

3. Experimental program

3.1. Material description and mechanical properties

The material utilized in the fracture tests described next is a typical ASTM A515 Grade 65 pressure vessel steel with 294 MPa yield stress and 514 MPa tensile strength at room temperature (20 °C) supplied as a hot rolled plate with 37.5 mm thickness. Mechanical tensile tests conducted on standard tensile specimens with 12.5 mm diameter extracted from the transverse plate direction provide the room temperature (T = 20 °C) stress–strain data. These test pieces were loaded in a 250 kN MTS servo-hydraulic universal testing machine with an axial extensometer to measure the specimen elongation according to ASTM E8M [36] requirements. Because fracture testing was conducted in the DBT region (see further details next), additional tensile tests were also conducted at different low temperatures, defined by $T = -10$ °C and $T = -20$ °C, on subsized test specimens with 6 mm diameter. Table 1 summarizes the tensile testing results for each test temperature which evidence the high hardening behavior of the tested steel with $\sigma_{uts}/\sigma_{ys} \approx 1.7 \sim 1.8$. Other mechanical properties for this material include Young's modulus, $E = 210$ GPa and Poisson's ratio, $\nu = 0.3$. Fig. 1(a) provides the engineering stress–strain curve for the ASTM A515 Grade 65 steel at room temperature (average stress–strain response using data from three standard test specimens) and also includes the true stress–logarithmic strain curves at test temperatures ($T = -10$ °C and $T = -20$ °C) for the material used in our finite element analyses of the fracture specimens addressed subsequently. For reference, an improved estimate for the hardening exponent given by Annex F of API 579 [1] provides the strain hardening exponents at the test temperatures (refer to Table 1) as $n = 6.4$ for $T = -10$ °C and $n = 6.6$ for $T = -20$ °C; these values are in accord with the behavior displayed in Fig. 1(a) in which the tensile response at $T = -20$ °C shows a slightly lower hardening characteristic than at $T = -10$ °C.

A series of Charpy Tests were performed at 8 different temperatures on standard V notch (CVN) impact specimens extracted in the TL plate orientation. This set of specimens was tested in a 360J full-scale Tinius-Olsen pendulum machine, following the requirements of ASTM E23 standard [37]. Fig. 1(b) shows the measured toughness-temperature properties for the material in terms of conventional Charpy V-notch impact energy (T-L orientation). In this plot, the symbols represent the

Table 1
Tensile properties of tested A515 Gr 65 steel at different test temperatures measured from transverse plate direction at mid-thickness location (σ_{ys} and σ_{uts} denote the yield stress and tensile strength while ϵ_t represents the uniform elongation for a gage length equals four times the specimen diameter as per ASTM E8M [36]).

T (°C)	σ_{ys} (MPa)	σ_{uts} (MPa)	σ_{uts}/σ_{ys}	n	e_t (%)
20	294	514	1.8	6.1	24
−10	313	527	1.7	6.4	n.a
−20	321	532	1.7	6.6	n.a

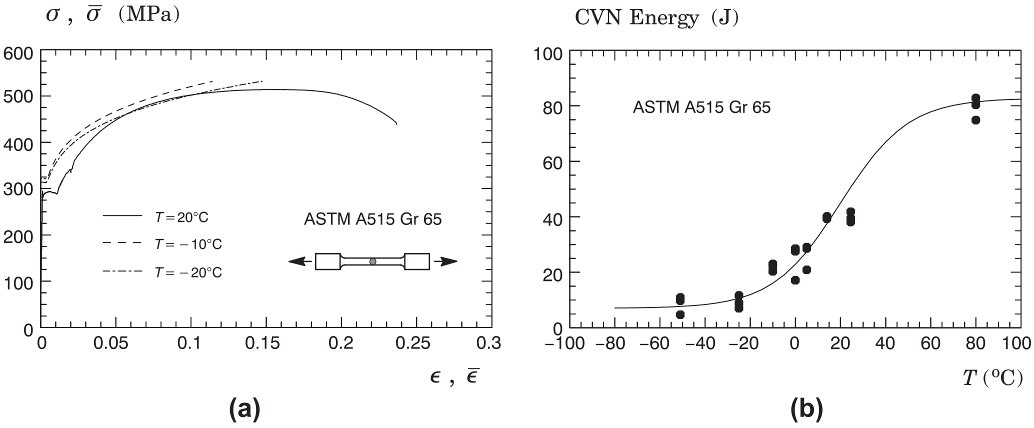

Fig. 1. Mechanical properties of tested A515 Gr 65 steel: (a) Average tensile response at different test temperatures (engineering and true stress–logarithmic strain properties) measured from transverse plate direction at mid-thickness location and (b) Charpy-V impact energy (T-L orientation) versus temperature.

experimentally measured Charpy energy and the solid line defines a hyperbolic tangent curve fitting proposed by Kirk et al. [38] in the form

$$CVE = 45 + 38\tanh\left[\frac{T-20}{30}\right] \tag{13}$$

where CVE denotes the Charpy V-notch energy expressed in J and T is the test temperature in degrees Celsius. Using the above expression, the Charpy transition temperature corresponding to a 28 J energy yields approximately $T_{CVN} = 6\,^{\circ}\mathrm{C}$.

3.2. Fracture toughness testing

Fracture toughness tests were performed on conventional, plane-sided three-point bend fracture specimens with varying crack sizes and specimen thickness in the T-L orientation. The fracture mechanics tests include: (1) conventional, plane-sided SE(B) specimens with $a/W = 0.15$ and $a/W = 0.5$, $B = 30$ mm, $W = 60$ mm and $S = 4W$, and (2) plane-sided, precracked Charpy (PCVN) specimen with $a/W = 0.5$, $B = 10$ mm, $W = 10$ mm and $S = 4W$. Here, a is the crack size, W denotes the specimen width, B represents the specimen thickness and S is the load span. ASTM E1820 [39] provides additional details for the geometry and dimensions of the tested fracture specimens.

Following the requirements of ASTM E1820 [39] and ASTM E1921 [40], a fatigue precrack was introduced at the machined notch root by cyclic loading the fracture specimens under three-point bending at room temperature. In particular, special care was exercised during the fatigue precracking of the PCVN geometries to ensure that the values of the stress intensity factor attained in the procedure and the amount of fatigue crack growth were fully in accordance with the requirements of ASTM E1921 [40]. Load vs. crack mouth opening displacements (CMOD) records for each specimen were measured using a clip gauge mounted on an integrated knife-edge machined into the notch mouth. The test specimens were immersed in a nitrogen/alcohol bath with temperature controlled by a thermocouple wired to a digital thermometer. The cooling bath temperature was then maintained during 20–30 min at the specified test temperature before the test specimens were loaded. Post-test examinations established the amount of fatigue crack growth to determine the initial crack size by adopting a 5-point measurement technique; the technique is very similar to the procedure described in ASTM E1820 [39], but with points along the crack front near the specimen surfaces omitted in the averaging process to avoid including points that exhibit almost no crack extension. A similar technique was employed to measure the amount of ductile tearing, if any, prior to final fracture by cleavage in the tested specimens.

Cleavage fracture toughness data in terms of J_c-values were determined from the estimation procedure based on η-factors given in ASTM E1820 [39] using the experimentally measured plastic area under the load-CMOD curve for each test specimen. Recent work by Souza and Ruggieri [41] shows that the estimation formulas given by ASTM E1820 [39] yield J_c-values in excellent agreement with the toughness values derived from using the η-factors based on 3-D finite element analysis, including the PCVN geometry; hence, the measured J_c-values characterize very well the cleavage fracture toughness behavior of the tested steel. Table 3 shows the fracture toughness at cleavage instability for the A515 Gr 65 steel obtained from fracture specimens with varying specimen geometries tested at two different temperatures ($T = -10\,^{\circ}\mathrm{C}$ and $T = -20\,^{\circ}\mathrm{C}$). The table also includes the average precrack fatigue length based on a 5-point measurement technique. Post-mortem examination of the fracture surfaces for the SE(B) specimens and PCVN geometry revealed essentially no ductile tearing prior to cleavage fracture. Fig. 3(a) displays a typical fracture surface for the SE(B) specimen with $a/W = 0.5$ at $-20\,^{\circ}\mathrm{C}$ showing no evidence of plastic deformation at the crack front and clear characteristics of brittle fracture – this corresponds to specimen number 6 in Table 3 with $J_c = 120$ kJ/m^2. Fig. 3(b) and (c) shows a scanning electron microscopy (SEM) for this fracture surface examined very close to the crack-tip region. Observe the relatively well-defined transition between the tip of the fatigue precrack and the beginning of the fracture surface shown in Fig. 3(b) for a relatively lower magnification while Fig. 3(c) clearly reveals well-defined cleavage planes characteristic of stress-controlled cleavage fracture at the same crack-tip region under a much larger magnification.

The cumulative Weibull distribution of the measured J_c-values for both test temperatures is displayed in Fig. 2. The solid symbols in the plots represent the experimentally measured fracture toughness (J_c)-values for each test specimen. The cumulative probability, $F(J_c)$, is derived by simply ranking the J_c-values in ascending order and using the median rank position defined in terms of $F(J_{c,k}) = (k - 0.3)/(N + 0.4)$, where k denotes the rank number and N defines the total number of experimental toughness values [13]. The fitting curves to the experimental data shown in this figure describe the three-parameter Weibull distribution [13] for J_c-values given by

$$F(J_c) = 1 - \exp\left[-\left(\frac{J_c - J_{\min}}{J_0 - J_{\min}}\right)^{\alpha}\right] \tag{14}$$

in which α defines the Weibull modulus (which characterizes the scatter in test data), J_0 is the characteristic toughness and $J_{\min}$ denotes the threshold J-value corresponding to a $K_{\min}$ of 20 MPa $\sqrt{\mathrm{m}}$. A parameter estimation of the data set shown in Fig. 2 is performed by adopting the maximum likelihood (ML) method with a fixed value of $\alpha = 2$ as the Weibull modulus of the Weibull distribution describing the J_c-values – the $\alpha = 2$ value characterizes well the scatter in cleavage fracture toughness data under small scale yielding conditions [42,43]. The ML estimate of the characteristic toughness, J_0, then yields $\widehat{J}_0 = 86$ kJ/m^2 for the SE(B) specimen with $a/W = 0.5$, $\widehat{J}_0 = 160$ kJ/m^2 for the SE(B) specimen with $a/W = 0.15$ and

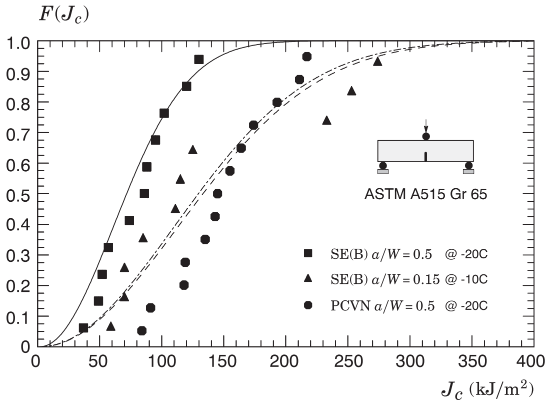

Fig. 2. Cumulative Weibull distribution of experimentally measured J_c-values for all tested specimen geometries.

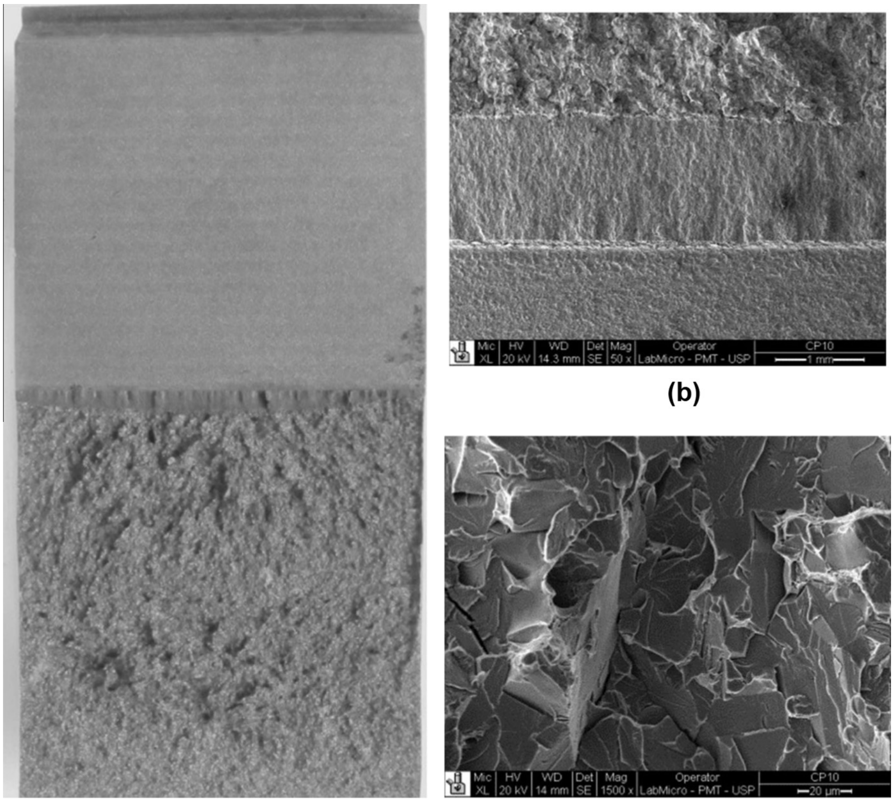

(b)

(a)

(c)

Fig. 3. (a) Typical fracture surface for the deeply-cracked specimen with $a/W = 0.5$ at $-20\,^{\circ}$C showing no evidence of plastic deformation at the crack front; (b) and (c) Scanning electron microscopy (SEM) of the fracture surface for the deeply-cracked specimen with $a/W = 0.5$ at $-20\,^{\circ}$C.

$\widehat{J}_0 = 155$ kJ/m^2 for the PCVN configuration. Table 2 provides the ML estimates of parameter J_0 for the measured distributions of J_c-values of each specimen geometry with a fixed value $\alpha = 2$, including the 90% confidence bounds for the characteristic toughness derived from Thoman et al. [44] (see also Mann et al. [13]).

The results shown in Fig. 2 and also in Table 2 reveal that the experimental toughness distributions for the tested fracture specimens follow a Weibull function with somewhat different α-values, particularly in the case of the PCVN configuration. Further investigation to understand the causes of the less-than-desirable fitting quality of the data to the Weibull distribution with $\alpha = 2$ suggested no evidence of potential deviations caused by the testing procedure nor any significant effects of ductile tearing on cleavage fracture toughness for these specimen geometries – as already noted before, our post-mortem examination of the fracture surfaces for the tested fracture specimens showed no apparent measurable amount of stable

Table 2
Maximum likelihood estimates of parameter J_0 for the measured distributions of J_c-values of each specimen geometry, including the 90% confidence bounds.

Geometry	T (°C)	ML estimates with fixed α		Standard ML estimates	
		α	J_0 (kJ/m^2)	α	J_0 (kJ/m^2)
SE(B) – $a/W = 0.5$	−20	2	86 (63, 117)	3.1	90 (75, 111)
SE(B) – $a/W = 0.15$	−10	2	160 (115, 223)	1.9	158 (114, 223)
PCVN	−20	2	155 (118, 205)	4.0	165 (145, 189)

crack growth. We may plausibly argue that the high hardening properties of the tested material allow the specimens to sustain higher J-values before cleavage fracture without nevertheless exhibiting any appreciable ductile tearing.

As will be seen later in Section 6, the toughness scaling procedure adopted in the present work enables the correction of the statistical distribution for fracture toughness data measured from two sets of test specimens exhibiting widely differing toughness behavior such as the characteristic toughness for one configuration is corrected for constraint effects to its equivalent characteristic toughness corresponding to other configurations. As further discussed in Section 6, the constraint corrections of interest are defined by $J_0^{SE(B)-a/W=0.15} \rightarrow J_0^{SE(B)-a/W=0.5}$ and $J_0^{PCVN} \rightarrow J_0^{SE(B)-a/W=0.5}$ at the same test temperature. Since the characteristic toughness, J_0, thus plays a key role in the Weibull stress parameter calibration and the constraint correction of toughness, it is of interest to inquire to what extent the quality of fitting affects the ML estimates of parameter J_0. To illustrate this issue, Table 2 also includes the ML estimates for the Weibull parameters, $\hat{\alpha}$ and $\widehat{J}_0$, including the 90% confidence bounds for J_0 [13,44], derived from a standard maximum likelihood estimation procedure [13] to determine *both* α and J_0. While the Weibull modulus does change (with respect to the fixed value of $\alpha = 2$) to reflect a decreased data scatter, the estimated J_0-value displays little sensitivity to the α-value; here, differences in J_0-estimates are $\approx 5\%$ for the deeply-cracked geometries and only $\approx 1\%$ for the shallow crack specimen with $a/W = 0.15$. Consequently, the degree of accord between the experimental data and the Weibull distribution described by Eq. (14) has little effect, if any, on the cleavage fracture predictions for the tested A515 steel addressed later in Section 6.

3.3. Evaluation of T_0 for the A515 Grade 65 steel

Valuable insights into the predictive capability of the proposed Weibull stress model can be gained from evaluation of the reference temperature, T_0, using fracture toughness measured using small-size fracture specimens as addressed later in Section 6. Without loss of generality, it provides a very representative case of specimen geometry effects on fracture toughness predictions against which the effectiveness of the $\tilde{\sigma}_w$-based methodology can be assessed. Before undertaking such an analysis, we first determine T_0 for the material under consideration using fundamental procedures.

The Master Curve method implemented into ASTM E1921 [8] and briefly presented in Appendix A is utilized in the present study to determine the reference temperature, T_0, for the tested A515 Gr 65 steel. The procedure evaluates T_0 from the fracture toughness distribution of J_c-values at $T = -20$ °C for the deeply-cracked SE(B) specimens converted to K_{Jc}-values using the standard relationship expressed by Eq. (A.2) provided in Appendix A. Moreover, since these fracture specimens have thickness $B = 30$ mm, these K_{Jc}-values are corrected to equivalent 1T size toughness values using simple weakest link statistics as also described in Appendix A.

Table 3 also shows the deformation (size) limit, M, which defines the measuring toughness capacity for each tested specimen. Clearly, all M-values (corresponding to the fracture toughness at cleavage instability defined by J_c) at $T = -20$ °C for the deeply-cracked SE(B) specimens are larger than the value $M = 60$ thereby ensuring toughness data associated with essentially stress-controlled failure by a transgranular cleavage mechanism under small scale yielding conditions [45] (note that ASTM E1921 [8] imposes a relatively less stringent condition for the maximum extension of plastic deformation by adopting the value $M = 30$). Thus, all measured K_{Jc}-values at $T = -20$ °C for the SE(B) specimens with $a/W = 0.5$ are considered valid tests. It is evident that, while we did not conduct additional fracture tests to assess the repeatability of the predicted reference temperature, this data set of J_c-values (K_{Jc}-values) should provide a credible estimate of T_0 and, consequently, the dependency of fracture toughness data on temperature over the DBT region.

For the tested pressure vessel steel, the reference temperature yields the value of $T_0 = -41$ °C which is 21 degrees below the test temperature. The dependence of fracture toughness on temperature over the DBT region for this material has thus the following form

$$K_{Jc-med} = 30 + 70\exp[0.019(T + 41)] \quad {}^\circ\text{C, MPa}\sqrt{\text{m}}. \tag{15}$$

Fig. 4 provides the variation of fracture toughness, described in terms of K_J, with temperature in which the solid line defines the master curve given by Eq. (15) and the dashed lines represent the 5% and 95% confidence bounds for the maximum likelihood estimate of K_0 – refer to the procedures to construct confidence bounds for the Master Curve analysis given by ASTM E1921 [8]. The measured K_{Jc}-values at $T = -20$ °C are included in the plot to aid in assessing the relative position of the master curve and, at the same time, the significance of the confidence bounds in enveloping the fracture toughness data. Moreover, a comparison of the results derived from the present master curve analysis with the measured Charpy energy data displayed in Fig. 1(b) reveals a marked difference between the indexing temperature ($T_0 = -41$ °C) and the Charpy transition temperature corresponding to a 28 J energy ($T_{CVN} \approx 6$ °C).

Table 3
Measured cleavage fracture toughness values, described in terms of J_c, for the A 515 Gr 65 steel obtained from fracture specimens with varying specimen geometries tested at two different temperatures.

Test temperature	Specimen geometry	Specimen number	J_c (kJ/m^2)	a_0 (mm)	$M = (b_0\sigma_{ys}/J_c)$
−20 °C	SE(B) $a/W = 0.5$	1	130	30.4	73
		2	88	30.2	109
		3	52	30.4	183
		4	95	30.2	101
		5	74	31.2	125
		6	120	30.5	79
		13	37	30.8	253
		14	86	30.4	110
		15	57	30.0	169
		16	49	30.9	191
		17	102	30.6	93
−10 °C	**SE(B)** $a/W = 0.15$	10	125	8.3	129
		11	253	7.8	65
		12	115	8.0	142
		13	111	8.0	147
		15	85	8.2	191
		16	274	8.6	59
		17	233	8.5	69
		18	70	8.1	232
		19	59	7.6	278
		20	70	8.4	231
−20 °C	PCVN	1	91	5.4	16
		2	217	5.1	7
		3	145	5.1	11
		4	135	5.0	12
		5	193	5.5	7
		6	211	5.3	7
		7	164	5.4	9
		8	118	5.1	13
		9	174	5.2	9
		10	155	5.2	10
		11	84	5.3	18
		12	119	5.3	13
		13	143	5.2	11

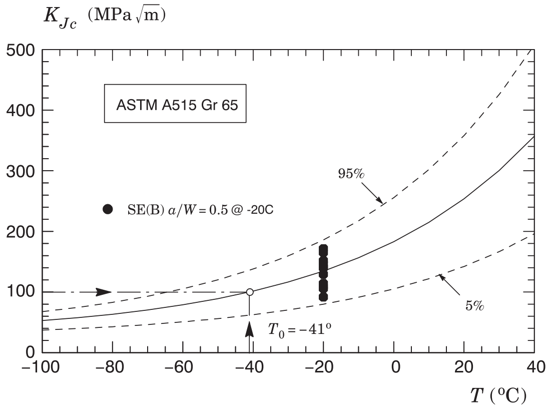

Fig. 4. Master curve for ASTM A515 Gr 65 steel including 5% and 95% confidence bounds based on cleavage fracture toughness values measured from standard SE(B) specimens with $a/W = 0.5$ and $B = 30$ mm.

4. Finite element procedures

4.1. Finite element models

Nonlinear finite element analyses are described for 3-D models of the tested SE(B) specimens with $a/W = 0.5$ and $a/W = 0.15$. These configurations have standard geometry ($W = 2B$ and $S = 4W$) with $B = 30$ mm and no side-grooves. Fig. 5(a) shows the typical finite element model utilized in the analyses of the deeply cracked SE(B) specimen with

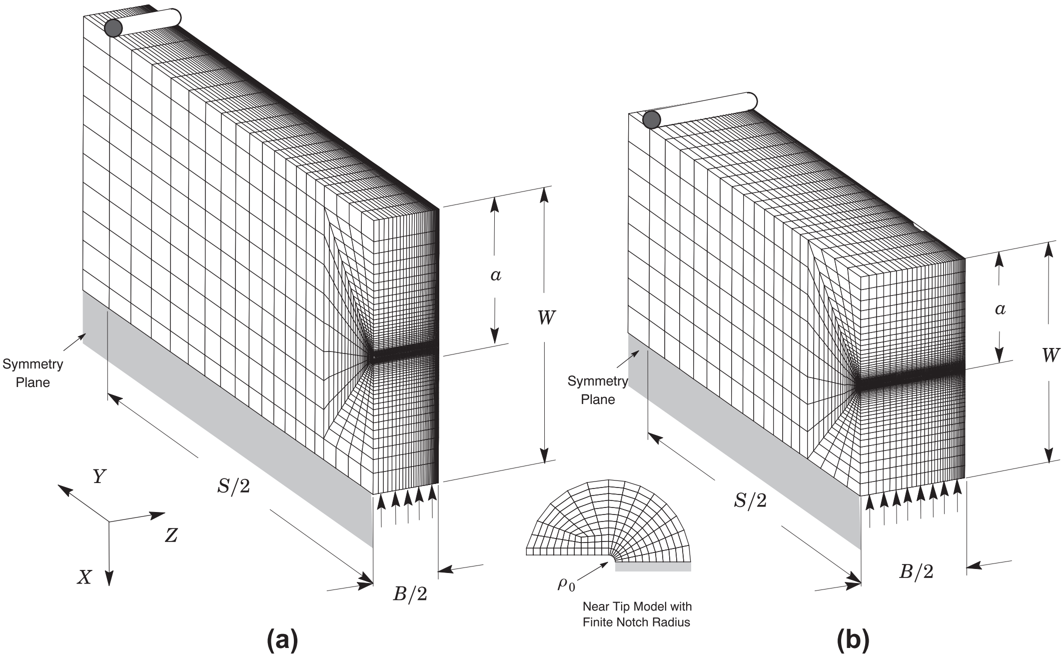

Fig. 5. Finite element models used in the 3-D analyses of the tested fracture geometries with $a/W = 0.5$: (a) SE(B) specimen with $B = 30$ mm and (b) PCVN geometry.

$a/W = 0.5$. With minor differences, the numerical model for the shallow crack SE(B) specimen with $a/W = 0.15$ has very similar features. A conventional mesh configuration having a focused ring of elements surrounding the crack front is used with a small key-hole at the crack tip; the radius of the key-hole, ρ_0, is 10 μm (0.01 mm). Symmetry conditions enable analyses using one-quarter of the 3-D models with appropriate constraints imposed on the symmetry planes. The mesh has 32 variable thickness layers defined over the half-thickness ($B/2$); the thickest layer is defined at $Z = 0$ with thinner layers defined near the free surface ($Z = B/2$) to accommodate strong Z variations in the stress distribution. The quarter-symmetric, 3-D model for this specimen has approximately 38,000 nodes and 34,000 elements. These finite element models are loaded by displacement increments imposed on the top nodes for the symmetry plane to enhance numerical convergence with increased loading and plastic deformation.

3-D finite element analyses are also conducted on a numerical model for the tested precracked Charpy (PCVN) specimen with $a/W = 0.5$. This finite element model has similar mesh arrangement and mesh details as already described for the SE(B) specimens. Fig. 5(b) shows the quarter-symmetric, 3-D model for this geometry with 22 variable thickness layers (approximately 27,000 8-node, 3-D elements and 31,000 nodes) defined over the half-thickness ($B/2$); the thickest layer is also defined at $Z = 0$ with thinner layers defined near the free surface ($Z = B/2$) to accommodate strong Z variations in the stress distribution. Again, this finite element model is loaded by displacement increments imposed on the top nodes for the symmetry plane.

4.2. Material relations and key solution procedures

The numerical solutions for the fracture toughness predictions based on the modified Weibull stress methodology described next utilize an elastic–plastic constitutive model with J_2 flow theory and conventional Mises plasticity in large geometry change (LGC) setting incorporating a piecewise linear approximation to the measured tensile response for the material. The mechanical and flow properties for the tested A515 Gr 65 are employed to generate the required numerical solutions at different temperatures. Section 3.1 provides details of the material properties adopted in the analyses, including the true stress–logarithmic strain curves at test temperatures ($T = -10$ °C and $T = -20$ °C).

The finite element code WARP3D [46] provides the numerical solutions for the 3-D analyses reported here. Fracture models are constructed with three-dimensional, 8-node hexahedral elements. The code formulates and solves the equilibrium equations at each iteration using parallel algorithms and implements the so-called $\overline{\mathbf{B}}$ formulation (see [46] for details) to preclude mesh lock-ups that arise as the deformation progresses into fully plastic, incompressible modes.

The local value of the mechanical energy release rate at a point along the crack front is given by [47]

$$J = \lim_{\Gamma\to 0}\int_{\Gamma}\left[W_s n_1 - \sigma_{ij}\frac{\partial u_i}{\partial x_1}n_j\right]d\Gamma \qquad (16)$$

where Γ denotes a contour defined in a plane normal to the crack front on the undeformed configuration beginning at the bottom crack face and ending on the top face, n_j is the outward normal to Γ, W_s denotes the stress-work density per unit of undeformed volume, σ_{ij} and u_i are Cartesian components of stress and displacement in the crack front coordinate system. The finite element computations employ a domain integral procedure [47] for numerical evaluation of Eq. (16) to provide pointwise and front average values of J across the crack front at each loading level. The thickness average values of J agree very well with estimation schemes based upon η-factors for deformation plasticity [48] so that they provide a convenient parameter to characterize the average intensity of far field loading on the crack front.

In the present methodology, a requisite feature to obtain nearly invariant $\tilde{\sigma}_w$-values at a fixed, specified macroscopic loading (as characterized by J) is to generate converged numerical descriptions of the crack-tip stress fields which are accurate over distances of order a few CTODs. A weak, implicit length-scale enters the finite element computations through the near-tip mesh size, as insufficient mesh refinement alters peak stress values ahead of the crack front, thereby potentially affecting the computed values of $\tilde{\sigma}_w$ – recall the Weibull stress calculation involves the principal stress raised to a large power defined by the Weibull modulus, m. However, extensive element distortion near the notch root prevents numerical convergence when too small notch root radii are used, particularly in the case of the shallow crack specimen and PCVN configuration loaded at higher J-values. Consequently, somewhat larger initial root radii are necessary to generate numerical solutions over the complete loading history for all analyzed fracture specimens. While the adopted mesh refinement (characterized by a blunting notch of $\rho_0 = 0.01$ mm) is perhaps slightly coarser than a more desirable higher refined mesh (as characterized by, for example, a blunting notch of $\rho_0 = 0.0025$ mm – see, for example, Gao et al. [16] and Petti and Dodds [20]), the 3-D models used in this study still possess the required level of mesh refinement to resolve accurately the crack-tip stress and strain to compute nearly invariant $\tilde{\sigma}_w$-values.

5. Specimen geometry effects on macroscopic fracture behavior

Before conducting verification studies to assess the effectiveness of the modified Weibull stress ($\tilde{\sigma}_w$) model to correct effects of constraint loss on fracture toughness addressed next, we first examine the influence of specimen geometry on macroscopic fracture behavior which has a bearing on the evolution of $\tilde{\sigma}_w$ with increased load levels for the deeply-cracked SE(B) and PCVN specimens considered in the present investigation. Since $\tilde{\sigma}_w$ derives directly from the integration of the near-tip stresses (and strains) over the crack front process zone, it is of interest to inquire to what extent the connection between the impingement of global bending field on a reduced specimen thickness and a smaller sampling volume for cleavage fracture affects its magnitude. Attention is directed to the changes in crack front driving force and crack front stress fields with increased macroscopic loading (as characterized by increased values of J in the present study) for the deeply-cracked SE(B) specimen with $B = 30$ mm and $W/B = 2$, and the PCVN configuration with $W/B = 1$. The analyses consider the material flow properties for the A515 Gr 65 steel corresponding to the test temperature, $T = -20$ °C.

5.1. Variation of the J-integral over the crack front

Fig. 6 displays the distribution of J over the crack front, denoted J_{local}, with increased load levels for the SE(B) and PCVN geometries. These J-values are normalized by the thickness average values, denoted J_{avg}, so that the ratio J_{local}/J_{avg} describes the variation of the local J-value relative to the thickness average J (recall that J_{avg} defines the conventional J-value that would be measured in fracture testing using a plastic η-factor as outlined previously in Section 3.2). In these plots, the deformation levels range from small-scale yielding conditions to fully yielded conditions and take the values, $J/(b\sigma_{ys}) = 0.010$,

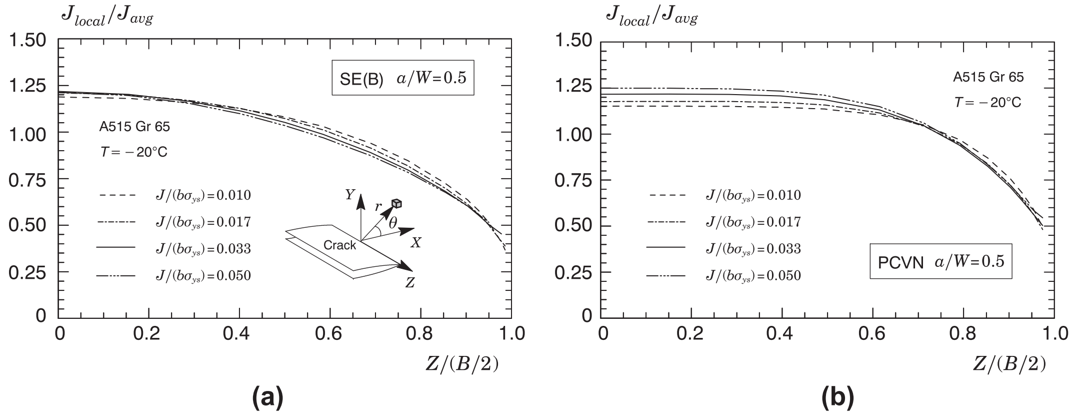

Fig. 6. Distribution of the J-integral over the crack front with increased deformation levels for the bend specimens at $T = -80$ °C: (a) SE(B) geometry with $a/W = 0.5$ and (b) PCVN configuration with $a/W = 0.5$.

0.017, 0.033 and 0.050. In particular, the values of $J/(b\sigma_{ys}) = 0.017$ and 0.033 correspond to a crack tip deformation limit of $M = 60$ and $M = 30$ relative to crack length, specimen thickness and remaining ligament.

The results shown in Fig. 6(a) corresponding to the SE(B) specimen reveal that the maximum J-values occurs over a relatively moderate-to-large portion of the specimen center plane region ($0 \leqslant Z/(B/2) \leqslant 0.4$) and then gradually decreases to much lower J-values as the stress-free surface is approached. For the PCVN configuration, the distributions of J across the specimen thickness shown in Fig. 6(b) becomes slightly more uniform for the entire range of deformation over a somewhat larger portion of the crack front as much as ($0 \leqslant Z/(B/2) \leqslant 0.6$). Nevalainen and Dodds [45] report similar results for bend geometries with $W/B = 1$ configuration.

5.2. Crack front stress triaxiality

Additional quantitative understanding of specimen geometry effects on the crack front stress fields can be gained by examining the evolution of crack front stress triaxiality with increased load level in terms of the $J - Q$ methodology [49–51,45], already briefly outlined in Part I of this work [11]. The $J - Q$ trajectories are generated at selected locations along the crack front for the SE(B) and PCVN fracture specimens as shown in Fig. 7. For reference, the first five layers closest to the specimen midplane displayed in these plots correspond to the locations: $Z/(B/2) = 0, 0.15, 0.3, 0.4$ and 0.5. Moreover, results derived from plane-strain analysis conducted for these configurations are also included for comparison; R&D [11] describe in more detail the numerical framework to conduct the plane-strain $J - Q$ trajectories. To maintain positive scales, we plot $J/(b\sigma_{ys})$ against negative values of Q in which parameter Q is calculated at the normalized distance ahead of crack tip given by $r/(J/\sigma_{ys}) = 2$ and J is normalized by $(b\sigma_{ys})$ with b denoting the remaining crack ligament, $W - a$. Further observe that the variation of Q along the crack front is plotted against increased macroscopic loading characterized in terms of thickness average value, J_{avg}.

The results displayed in Fig. 7 reveal that the evolution of Q as loading progresses displays strong dependence on the crack front location. For both geometries, the highest constraint levels are maintained at the specimen midplane. Due to the nonuniform distribution of deformation over the thickness elevated in the midplane region, the 3-D models continue to maintain high levels of constraint compared to the plane-strain model where each location along the crack-front has identical deformation. Observe that the Q-values for the first two layers closest to the specimen midplane for the deeply-cracked SE(B) specimen ($Z/(B/2) = 0$ and 0.15) are slightly higher than the Q-values at the specimen midplane for the PCVN configuration. Further observe that the $J - Q$ trajectories for the first three layers of the PCVN specimen ($Z/(B/2) = 0, 0.15, 0.3$) match very well the $J - Q$ trajectory corresponding to the third layer ($Z/(B/2) = 0.3$) of the SE(B) specimen.

Much of the difference in cleavage fracture behavior exhibited by the toughness testing of deeply-cracked SE(B) and PCVN specimens described in Section 3.2 can be explained in terms of the results shown in Fig. 7. While the levels of crack front constraint at the specimen midplane for both configurations are comparable, their highly stressed near-tip fracture process zones differ largely in spatial size. To keep things simple, consider first the deeply-cracked SE(B) specimen for which the highest $J - Q$ trajectories span over the range $0 \leqslant Z/(B/2) \leqslant 0.3$ which is equivalent to a crack front thickness of ≈ 9 mm. Consider now the PCVN geometry for which the highest $J - Q$ trajectories span over the same range $0 \leqslant Z/(B/2) \leqslant 0.3$ which is equivalent to a crack front thickness of ≈ 3 mm. Thus, a strong statistical effect arises in the case of the PCVN configuration (associated with a much smaller sampling volume ahead of the crack front) which clearly offsets the relatively increased constraint levels at the specimen midplane. These arguments can be confirmed by inspecting Fig. 2 and Table 2 in which the PCVN configuration exhibits significant elevation (factors of ~ 2) in J_c-values relative to the deeply-cracked SE(B) specimen tested at the same temperature. The following section addresses the evolution of crack front principal stress zones with

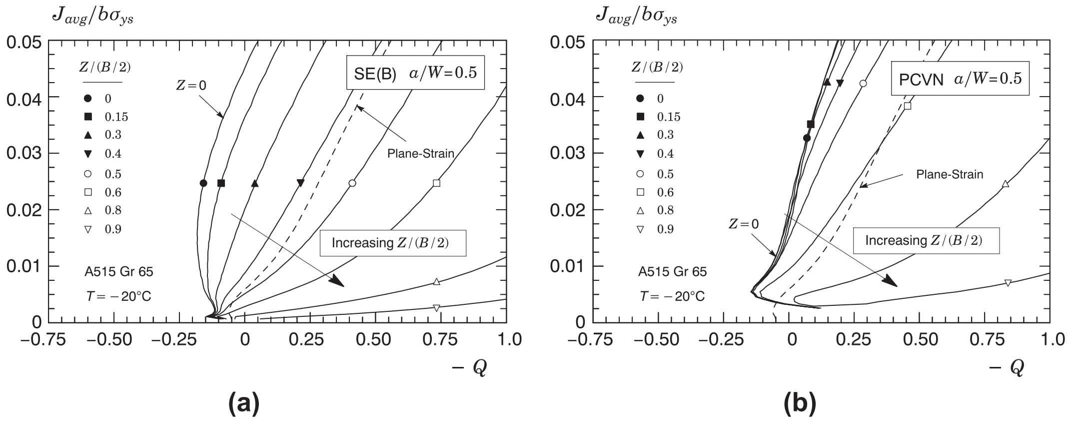

Fig. 7. $J - Q$ trajectories at locations along the crack front for the bend specimens at $T = -80$ °C: (a) SE(B) geometry with $a/W = 0.5$ and (b) PCVN configuration with $a/W = 0.5$.

increased load levels for these specimens which provides additional support to the observed differences in their cleavage fracture behavior.

5.3. Crack front principal stress zones

Figs. 8 and 9 show the contour maps of the maximum principal stress, σ_1, for which $\sigma_1 \geqslant 2\sigma_{ys}$ at the specimen midplane and over the crack front for the deeply-cracked SE(B) specimen and PCVN configuration at two widely distinct levels of loading, $J/(b\sigma_0) = 0.017$ ($M = 60$) and $J/(b\sigma_0) = 0.033$ ($M = 30$). In the context of these geometries, the first load level corresponds to well-contained yielding whereas the latter load level, while still defining conditions similar to small-scale yielding, plausibly marks the transition to a fully yielded state. Moreover, to the extent that the cleavage fracture process can be assumed as a stress-controlled fracture mechanism, the near-tip region associated with the spatial extent of the stress contour defined by $\sigma_1 \geqslant 2\sigma_{ys}$ provides a quantitative measure of the fracture process zone of a few CTODs ahead of the macroscopic crack. A graphical scale is also provided on the figures to aid in assessing the relative spatial extent of the principal stress zones.

Consider first the principal stress contours for the deeply-cracked SE(B) specimen displayed in Fig. 8. Under contained yielded state corresponding to $M = 60$, a high stress zone is already well developed and has spread across a large portion of the crack ligament. With increased loading corresponding to a deformation level of $M = 30$, the size of the high stress zones grows even further and extends its linear dimension by nearly 30%. Observe that the size of the zone where σ_1 exceeds σ_{ys} over the crack front shown in Fig. 8(b) and (d) is significantly larger over a relatively small fraction of the specimen thickness extending from midplane and then gradually decreasing as the stress-free surface is approached.

Now direct attention to the results for the PCVN specimen shown in Fig. 9. While the general development of the crack front principal stress fields is broadly consistent with the principal stress distributions shown in previous Fig. 8, the size and spatial extent of the distribution of σ_1 over the crack front for the PCVN geometry contrast markedly with those for the deeply-cracked SE(B) specimen. Indeed, the linear dimensions of the principal stress contours for the PCVN geometry are

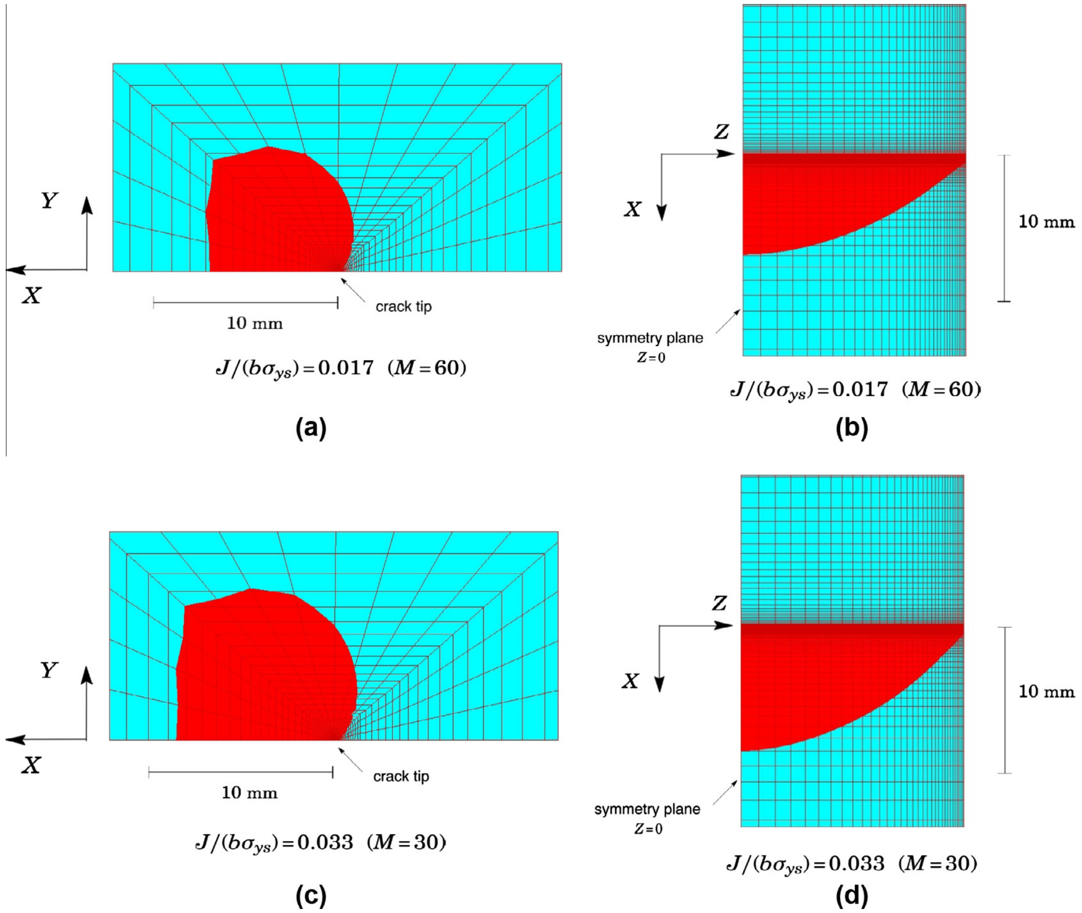

Fig. 8. Maximum principal stress zones for which $\sigma_1 \geqslant 2\sigma_{ys}$ for the deeply-cracked SE(B) specimen at two widely distinct levels of loading: (a) and (b) Contour of principal stress at $J/(b\sigma_0) = 0.017$; (c) and (d) contour of principal stress at $J/(b\sigma_0) = 0.033$.

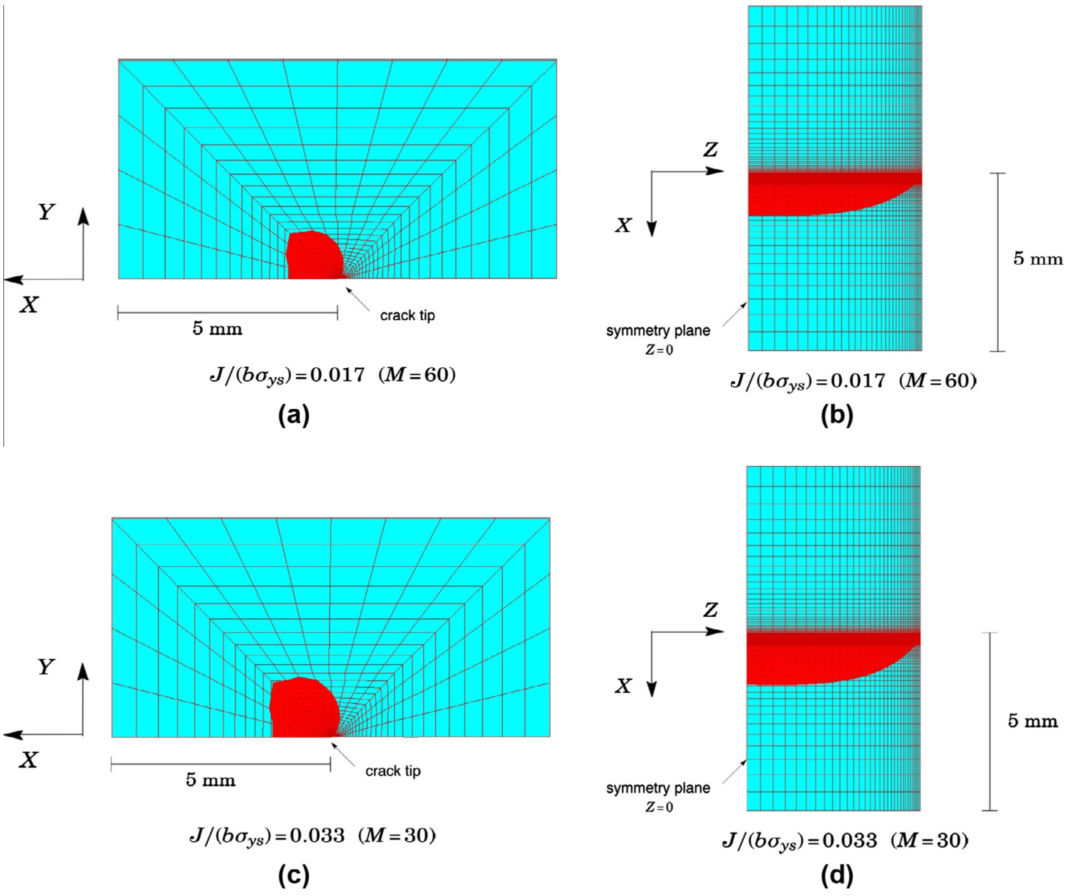

Fig. 9. Maximum principal stress zones for which $\sigma_1 \geqslant 2\sigma_{ys}$ for the PCVN geometry at two widely distinct levels of loading: (a) and (b) Contour of principal stress at $J/(b\sigma_0) = 0.017$; (c) and (d) contour of principal stress at $J/(b\sigma_0) = 0.033$.

reduced by approximately one-third as indicated by the scale of the plots. Further observe that the size of the zone where σ_1 exceeds σ_{ys} over the crack front for this configuration remains relatively unchanged with increased load levels; here, the principal stress contours corresponding to $M = 30$ are only slightly larger than those for the deformation level of $M = 60$.

The results displayed in Figs. 8 and 9 have a direct bearing on the fracture toughness behavior exhibited by the tested specimens described in Section 3.2. Further, they also provide a compelling case for using the toughness scaling methodology based on a modified form of the Weibull stress incorporating effects of plastic strain adopted in the present investigation. As already discussed, the toughness scaling model requires the attainment of a specified value for $\tilde{\sigma}_w$ to trigger cleavage fracture across different crack configurations even though the loading parameter (as characterized by the J-integral) may vary widely due to constraint loss. For the tested fracture specimens under consideration, the crack front stress distribution (which also defines the size and spatial extent of the near-tip fracture process zone) is strongly dependent on geometry so that the deeply-cracked SE(B) specimen permits the persistence of the maximum principal stress buildup (with increased loading) whereas the PCVN specimen does not. Clearly, the much larger highly stressed sampling volume ahead of the crack front for the SE(B) geometry provides much more favorable conditions to trigger unstable cleavage fracture at lower J-values. By contrast, a similar principal stress buildup does not occur on the PCVN geometry (compare Figs. 8 and 9) so that it may never be possible to meet the conditions for triggering unstable cleavage fracture at lower levels of applied loading as this would require a marked increase in the volume of the fracture process zone ahead of the crack front, and hence a large likelihood of a high stress zone sampling a cleavage microcrack. Thus, fracture toughness constraint corrections, $J_{PCVN} \rightarrow J_{SEB}$, based on the standard Beremin model tend to underpredict fracture toughness for larger specimens on the basis of toughness values from smaller geometries – indeed, this is precisely the result obtained later in Section 6.

Another further aspect of the results shown in Figs. 8 and 9 underscores the limitations of simple weakest link statistics to predict the absolute effects of thickness on fracture toughness. As already discussed in Part I of this work [11], it is possible to demonstrate based on purely statistical arguments that the fracture toughness for specimens with similar geometries and same a/W will decrease proportionally to $B^{-1/\alpha}$ as the thickness, B, increases with α denoting the modulus of the Weibull distribution describing the fracture toughness. ASTM E1921 [40] (and other similar procedures as well) adopt weakest link arguments to correct K_{Jc}-values for similar fracture specimens with different thicknesses in the form of Eq. (A.3) provided in Appendix A. That expression thus implies that each point along the crack front for both specimen geometries experiences the same local crack driving force value and, most importantly, the same local stress field. The previous results clearly reveal a different picture in which: (1) the actual specimen thickness which quantifies the actual portion of crack front length over which the near-tip stresses reach levels sufficiently high to trigger cleavage fracture differs for each geometry and (2) even at the front location at which the maximum in-plane constraint takes place (which corresponds to the midplane region for both geometries), the levels of near-tip stresses for the deeply-cracked SE(B) specimen and PCVN configuration, as quantified by their $J-Q$ trajectories (refer to previous Fig. 7), are somewhat dependent on the specimen geometry. Nevalainen and Dodds [45] have addressed this issue to propose an effective thickness, B_{eff}, entering into Eq. (A.3), rather than the actual specimen thickness, to correct fracture toughness values for thickness effects. The concept of B_{eff} alleviates the often observed under-correction of measured toughness values associated with straightforward application of Eq. (A.3) in which the actual specimen thickness is used. The procedure, however, does not take account of the individual contribution of all material points along the crack front into the total failure probability since it attributes equal weight to these material volumes. These features, taken together with the above discussions, support the adoption of a more refined formulation for the Weibull stress in which the coupling of constraint loss and plastic strain effects offsets the influence of a relatively small zone of high principal stress that develops in the PCVN configuration on the fracture toughness constraint corrections as addressed next.

6. Cleavage fracture predictions using the modified Weibull stress

6.1. Effects of plastic strain on Weibull stress trajectories

Before launching into the analysis of specimen geometry effects on cleavage fracture using the modified Weibull stress model, we briefly examine the influence of plastic strain on the $\tilde{\sigma}_w$-trajectories for the deep and shallow crack SE(B) configurations. A central objective is to gain some understanding on the role of plastic strain on the evolution of $\tilde{\sigma}_w$ (interpreted as a probabilistic crack driving force in the present context) with J by means of varying key plastic strain parameters (which are related to the function Ψ_c). In the analyses to be discussed, the Weibull modulus has a fixed value of $m = 10$, which compares well to previously reported m-values for structural steels with similar hardening behavior [16,52]. Indeed, the adopted $m = 10$ value is very close to the calibrated Weibull modulus for the tested A515 steel addressed next. Moreover, the material properties correspond to the measured tensile response at $T = -10\,^\circ$C.

Figs. 10 and 11 compare the evolution of $\tilde{\sigma}_w/\sigma_{ys}$ with increased loading for $\tilde{\sigma}_w$ expressed by previous Eqs. (5) and (8), which correspond to the simplified particle distribution and the exponential dependence models. These plots illustrate the effects on parameters σ_{prs} and λ on the modified Weibull stress trajectories and also compare the influence of specimen geometry on the $\tilde{\sigma}_w$ vs. J curves. The Weibull stress trajectories derived from the standard Beremin model are also provided on the figures to aid in assessing the effects of plastic strain on $\tilde{\sigma}_w$.

Consider first the deep crack results shown in Fig. 10(a) and (b). The significant features include: (1) For a given load level, as characterized by the J-integral, inclusion of plastic strain effects decrease the Weibull stress to levels below the corresponding levels for the standard Beremin model (which does not consider plastic strain effects). (2) The $\tilde{\sigma}_w$-trajectories for the simplified particle distribution model display more sensitivity to the key parameter σ_{prs}; here, $\tilde{\sigma}_w$ decreases relative to the standard Beremin model with increased σ_{prs}-values. (3) The $\tilde{\sigma}_w$-trajectories for the exponential dependence model are less dependent on the key parameter λ.

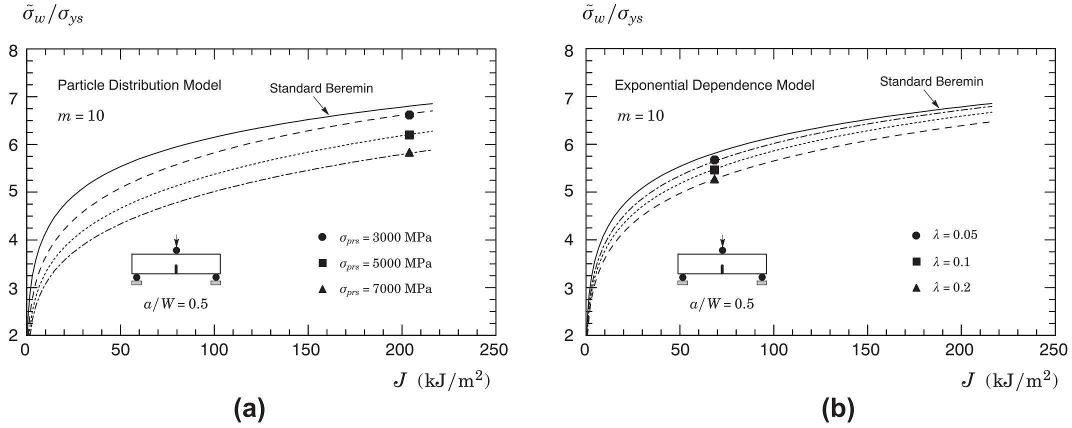

Fig. 10. Evolution of $\tilde{\sigma}_w/\sigma_0$ with increased loading for the deeply-cracked SE(B) specimen ($a/W = 0.5$) incorporating effects of plastic strain with $m = 10$ and material properties at $T = -10\,^\circ$C: (a) Simplified particle distribution model with $\sigma_{prs} = 3000$, 5000 and 700 MPa; (b) exponential dependence model with $\lambda = 0.05$, 0.1 and 0.2.

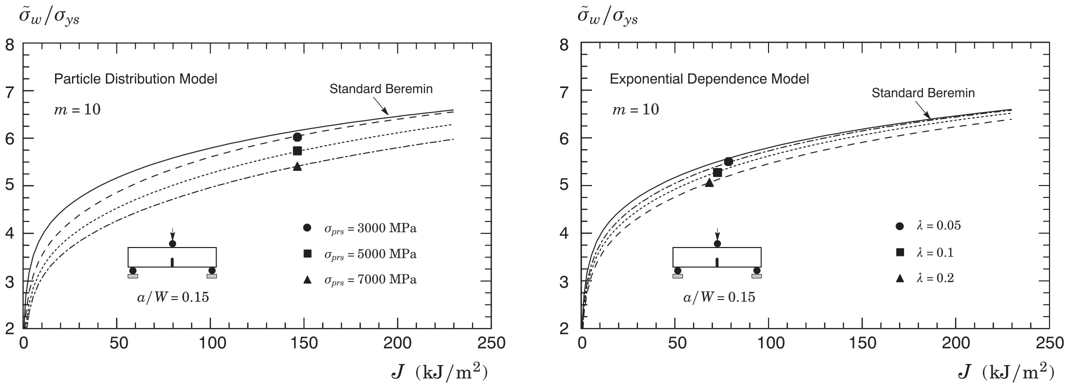

(a) **(b)**

Fig. 11. Evolution of $\tilde{\sigma}_w/\sigma_0$ with increased loading for the shallow crack SE(B) specimen ($aW = 0.15$) incorporating effects of plastic strain with $m = 10$ and material properties at $T = -10\,^\circ$C: (a) Simplified particle distribution model with $\sigma_{prs} = 3000$, 5000 and 700 MPa; (b) exponential dependence model with $\lambda = 0.05$, 0.1 and 0.2.

Consider next the shallow crack results displayed in Fig. 11(a) and (b). The overall trends remain similar except that the levels of $\tilde{\sigma}_w$ relative to corresponding levels for the deeply-cracked geometry are lower due to constraint loss experienced by the shallow crack specimen. Moreover, observe that the key parameter σ_{prs} plays a slightly lesser role in altering the $\tilde{\sigma}_w$ vs. J curves for simplified particle distribution. Essentially similar results are obtained for other analyses employing different m-values – to conserve space, they are not shown here.

6.2. Calibration of the modified Weibull stress parameters

Application of the modified Weibull stress methodology outlined above requires correct specification of the m-value and the function Ψ_c entering directly into the calculation of $\tilde{\sigma}_w$ through Eq. (2). The m-parameter and Ψ_c thus play a crucial role in defining the $\tilde{\sigma}_w$-trajectories for each specimen geometry upon which the toughness correction for constraint loss is derived. Since the Weibull modulus, m, characterizes the distribution of Griffith-like microcracks associated with the cleavage fracture process (see Ruggieri and Dodds [11] and references therein), we can advantageously evaluate m and Ψ_c using a two-step process as follows.

First, parameter m is determined to establish the best correction for cleavage fracture toughness data measured from two sets of test specimens exhibiting largely contrasting toughness behavior based on the standard Beremin model (i.e., $\Psi_c = 1$). The procedure essentially relies on the toughness scaling model (TSM) proposed earlier by Ruggieri and Dodds [53] building upon the interpretation of $\tilde{\sigma}_w$ as the (probabilistic) crack tip driving force coupled with the condition that cleavage fracture occurs when $\tilde{\sigma}_w$ reaches a critical value, $\tilde{\sigma}_{w,c}$. For the same material at temperatures within the DBT region and sufficiently close to the test temperature, the scaling model requires the attainment of a specified value for $\tilde{\sigma}_w$ to trigger cleavage fracture across different crack configurations even though the loading parameter (measured here by the J-integral) may vary widely due to constraint loss. Once the relation between the Weibull stress ($\tilde{\sigma}_w$) and applied loading (J) for a given value of the Weibull modulus, m, is determined, the calibration scheme adopted here defines the calibrated Weibull modulus for the material as the m-value, denoted m_0, that corrects the characteristic toughness J_0^B corresponding to a low constraint configuration (denoted as configuration **B**) to its equivalent J_0^A corresponding to a high constraint configuration (denoted as configuration **A**) such that the residual toughness values defined as $R(m) = (J_{0,m}^A - J_0^A)/J_0^A$ is minimized. Here, $J_{0,m}^A$ has an evident interpretation as the corrected characteristic toughness, J_0^A, derived from the $\tilde{\sigma}_w - J$ relation for a given value of the Weibull modulus, m. Gao et al. [16] and Ruggieri [35] discuss additional details of the calibration process for the Weibull modulus.

With the Weibull modulus (and, presumably, the microcrack distribution) thus determined and now assumed fixed throughout the analysis, the calibration process then proceeds by evaluation of the function Ψ_c that again provides the best correction for cleavage fracture toughness data measured from the two sets of test specimens utilized at the onset of the calibration procedure using the toughness scaling model. Here, the $\tilde{\sigma}_w - J$ relations for a fixed m_0-value enable determination of a Ψ_c that provides the best correction $J_0^B \rightarrow J_0^A$ such that the residual, $R(\Psi_c)$, is minimized. The calibrated values for m and Ψ_c clearly do not constitute a unique pair of parameters; for example, a slightly different m-value may be compensated for by a different Ψ_c. Nevertheless, the procedure is relatively simple and, perhaps most importantly, does preserve the character of parameter m in describing the microcrack distribution. Moreover, it is well to keep in mind that, within the present context, the calibrated Weibull parameter, m, is only loosely connected to the *actual* microcrack distribution. Because of the nature of the calibration process adopted here, which relies on the TSM and macroscopic measures of fracture toughness, m

and Ψ_c should be interpreted as *phenomenological* parameters that bring fracture toughness predictions into agreement, rather than accurate descriptors of the metallurgical features.

In the present application, calibration of parameter m is conducted at the test temperature, $T = -10\,^\circ\mathrm{C}$, by scaling the characteristic toughness of the measured toughness distribution for the shallow crack SE(B) specimen with $a/W = 0.15$ (taken here as configuration **B**) to the equivalent characteristic toughness of the toughness distribution for the deeply-cracked SE(B) specimen with $a/W = 0.5$. The research code WSTRESS [54] is utilized to compute $\tilde{\sigma}_w$ vs. J trajectories and to calibrate the Weibull modulus, m for the tested A515 steel based on the standard Beremin model (i.e., $\Psi_c = 1$ as already noted). However, because the specimens were not tested at the same temperature, the present methodology adopts a simple procedure to correct the measured toughness values for temperature using the Master Curve fitting given previously in Section 3.3. Since our primary interest lies in the calibration of the Weibull stress parameter and subsequent fracture toughness predictions, the approach provides sufficiently good estimates of fracture toughness at different temperatures without making recourse to an additional data set of toughness values. Here, the toughness distribution for the deeply-cracked SE(B) specimen at $T = -20\,^\circ\mathrm{C}$ is corrected to the corresponding toughness distribution at $T = -10\,^\circ\mathrm{C}$ thereby enabling direct application of the calibration methodology outlined above in which the characteristic toughness for the shallow crack SE(B) specimen, $J_0^{SEB-a/W=0.15}$, is corrected to its equivalent characteristic toughness for the deeply-cracked SE(B) specimen, $J_0^{SEB-a/W=0.5}$. The characteristic toughness value for the latter configuration at $T = -10\,^\circ\mathrm{C}$ then yields $J_0^{SEB-a/W=0.5} = 115\ \mathrm{kJ/m^2}$ – recall from Section 3.2 that $J_0^{SEB-a/W=0.15} = 155\ \mathrm{kJ/m^2}$ so that the toughness ratio $J_{SEB}^{a/W=0.15}/J_{SEB}^{a/W=0.5}$ at $T = -10\,^\circ\mathrm{C}$ is about ~ 1.4. The calibrated Weibull modulus then yields a value of $m_0 = 11$ which is well within the range of previously reported m-values for common pressure vessel and structural steels (see, e.g., [12,53,16,55,56]). Fig. 12 display the $\tilde{\sigma}_w$ vs. J trajectories based on the standard Beremin model with $m_0 = 11$ for both specimen geometries at the test temperature, $T = -10\,^\circ\mathrm{C}$. In these plots, $\tilde{\sigma}_w$ is normalized by the material yield stress, σ_{ys} – refer to Table 1. While a larger toughness ratio of $J_{SEB}^{a/W=0.15}/J_{SEB}^{a/W=0.5} \geqslant 1.6 \sim 1.8$ would be more desirable, the constraint difference between these two specimen geometries appears sufficiently large enough to provide an accurate calibrated m-parameter given the high hardening behavior of the A515 steel used in the present investigation. As already discussed in previous Section 3.2, the high hardening properties of the tested material allow the shallow crack bend specimens to sustain increased toughness measuring capacity in terms of J_c-values compared to similar geometries made of low hardening materials.

Calibration of the function Ψ_c in previous Eqs. (5), (8) and (9) follows from determining parameters σ_{prs}, λ and β that give the best correction of measured toughness values at $T = -10\,^\circ\mathrm{C}$ for the shallow and deep crack SE(B) specimens with a fixed value $m_0 = 11$. Here, we note that application of the modified Beremin Weibull stress is straightforward as no additional parameter calibration is needed – refer to Section 2.4. To illustrate the calibration process, Fig. 13(a) and (b) provides the constraint correlations $(J_{SEB}^{a/W=0.15} \to J_{SEB}^{a/W=0.5})$ for varying values of parameters σ_{prs} and λ. Each curve provides pairs of J-values in the shallow and deep crack SE(B) specimens which produce the same Weibull stress, $\tilde{\sigma}_w$, for a fixed σ_{prs}-value, when Ψ_c describes the simplified particle distribution model while holding fixed $\alpha_p = 4$ and $E_d = 400$ GPa, or a fixed λ-value, when Ψ_c describes the exponential dependence model. Further, within the present context of probabilistic fracture mechanics, each pair $(J_{SEB}^{a/W=0.15}, J_{SEB}^{a/W=0.5})$ on a given curve defines equal failure probabilities for cleavage fracture. A reference line is shown which defines a unit toughness ratio defined by $J_{SEB}^{a/W=0.15} = J_{SEB}^{a/W=0.5}$. Both parameters σ_{prs} and λ clearly affect the resulting toughness ratios for the deep and shallow crack bend configurations. In the plots shown in Fig. 13(a) and (b), correcting the characteristic toughness for the shallow crack SE(B) specimen, $J_0^{SEB-a/W=0.15}$, to its equivalent characteristic toughness for the deeply-cracked SE(B) specimen, $J_0^{SEB-a/W=0.5}$, then yields $\sigma_{prs} = 6500$ MPa and $\lambda = 0.03$. Table 4 provides these calibrated values for the tested material based on these different definitions for $\tilde{\sigma}_w$.

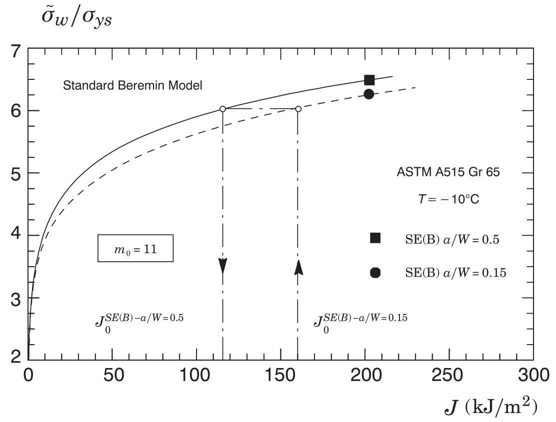

Fig. 12. $\tilde{\sigma}_w$ vs. J trajectories for the shallow and deeply-cracked SE(B) specimens at $T = -10\,^\circ\mathrm{C}$ based on the standard Beremin model with $m_0 = 11$.

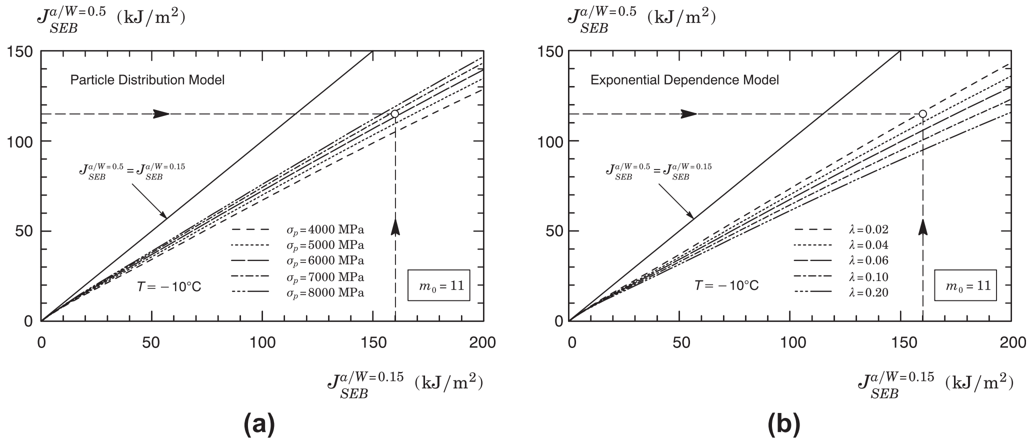

Fig. 13. Constraint correlations of J-values at $T = -10\,°\mathrm{C}$ for $m_0 = 11$: (a) Simplified particle distribution (WL) model with varying σ_{prs}-values; (b) exponential dependence model with varying λ-values.

Table 4
Calibrated Weibull modulus, m, and predicted J_0 and T_0-values for varying forms of Ψ_c.

Ψ_c	Primary parameter	Weibull parameter m	SE(B) $a/W = 0.5$ J_0 (kJ/m^2)	T_0 (°C)
Standard Beremin	n.a	11	47	−20
Modified Beremin	n.a	11	42	−16
Microcrack Density	$\beta = 0.2$	11	50	−22
Exponential Dependence	$\lambda = 0.03$	11	65	−32
WL $\alpha_p = 4$	$\sigma_{prs} = 6500$ MPa	11	87	−42

Further observe that the constraint correlations $J_{SEB}^{a/W=0.15} \to J_{SEB}^{a/W=0.5}$ shown in Fig. 13 hold a linear relationship for varying values of parameters σ_{prs} and λ. This behavior can be understood in terms of the plastic strain influence on $\tilde{\sigma}_w$ characterized by the function Ψ_c for both models. Under increased loading, the evolving constraint loss in the shallow crack specimen reduces the near-tip opening stresses while, at the same time, increasing the strain levels well inside the fracture process zone. In contrast, the deeply-cracked geometry maintains higher near-tip opening stresses and relatively lower strains with increased loading. Thus, the potentially stronger effects of constraint loss on $\tilde{\sigma}_w$ for the shallow crack specimen (compared to the deeply-cracked geometry) are (at least partly) balanced by its increased levels of plastic strains through Ψ_c. For fixed values of parameters σ_{prs} and λ, this translates into the linear relationship for the constraint ratio defined by $J_{SEB}^{a/W=0.5}/J_{SEB}^{a/W=0.15}$.

6.3. Prediction of specimen geometry effects on fracture toughness

To verify the predictive capability of the modified Weibull stress methodology adopted in the present work, this section describes applications of the $\tilde{\sigma}_w$-based approach to predict effects of geometry and constraint loss on cleavage fracture toughness values (J_c) for an A515Gr 65 pressure vessel steel. The notion of the modified Weibull stress as a crack-tip driving force establishes a function of the applied load and geometry which describes the local, crack-tip response for cleavage fracture. By postulating a critical value of the Weibull stress at fracture, $\tilde{\sigma}_{w,c}$, the distribution of measured toughness values for one configuration may then be rationally employed to predict toughness distributions for other configurations. Here, we predict the measured distribution of cleavage fracture values for the deeply-cracked SE(B) specimen ($a/W = 0.5$) with $B = 30$ mm using the measured fracture toughness distribution for the PCVN geometry, both tested at $T = -20\,°\mathrm{C}$ as already described in previous Section 3.2. The correlative procedure to obtain the toughness correction $J_0^{PCVN} \to J_0^{SE(B)-a/W=0.5}$ follows similar protocol for the toughness scaling methodology outlined previously. As already noted, the calibrated Weibull modulus is assumed as a material property at temperatures within the DBT region and sufficiently close to the test temperature.

Table 4 provides predictions of the characteristic fracture toughness, $J_0^{SE(B)-a/W=0.5}$, predicted from the present model. To facilitate comparisons, the analysis also includes the toughness values predicted from using the standard and the modified Beremin model. The agreement with the experimental characteristic toughness is remarkably close for the simplified particle distribution model with $\sigma_{prs} = 6500$ MPa – recall from Section 3.2 that $\widehat{J}_0^{SE(B)-a/W=0.5} = 86$ kJ/m^2. In contrast, the analysis using other models underpredicts the characteristic toughness for the deeply-cracked SE(B) specimen. In particular, the standard and the modified Beremin models yield the lowest estimates for the characteristic toughness for this geometry.

The $\tilde{\sigma}_w$ vs. J trajectories for $m_0 = 11$ corresponding to the simplified particle distribution and exponential dependence model with the calibrated Ψ_c displayed in Fig. 14(a-b) further illustrates the predictive response of the modified Weibull

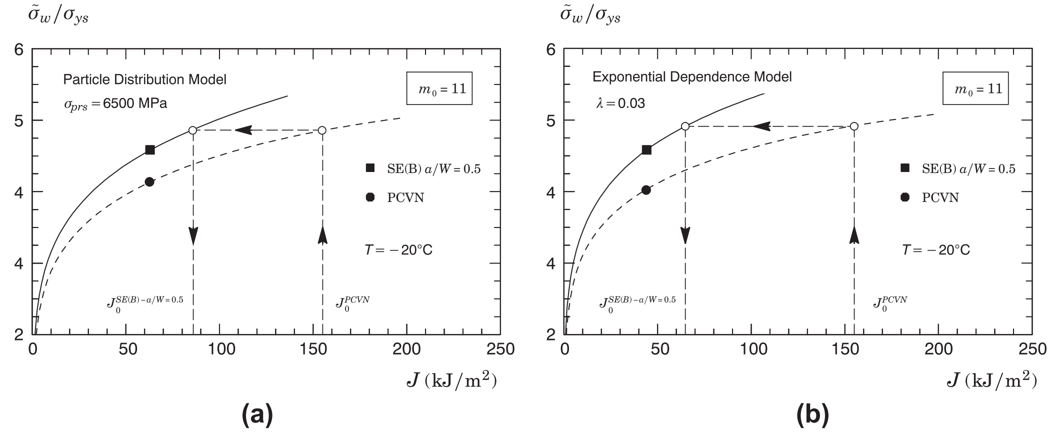

Fig. 14. Evolution of $\tilde{\sigma}_w$ with J for the deeply-cracked SE(B) specimen and PCVN configuration at $T = -20$ °C for $m_0 = 11$: (a) Simplified particle distribution (WL) model with $\sigma_{prs} = 6500$ MPa; (b) exponential dependence model with $\lambda = 0.03$.

stress model. In these plots, $\tilde{\sigma}_w$ is normalized by the material yield stress, σ_{ys}, at $T = -20$ °C – refer to Table 1. Observe that the $\tilde{\sigma}_w$ vs. J curves for the simplified particle distribution model differ in magnitude from the corresponding trajectories for the exponential dependence model thereby yielding different fracture toughness ratios, $J_0^{PCVN}/J_0^{SE(B)-a/W=0.5}$ as indicated in the plots.

The prediction of the cumulative probability distribution for fracture toughness data of the deeply-cracked SE(B) geometry and how it compares with the experimental data is also of interest. Fig. 15(a–d) shows the Weibull cumulative distribution function of J_c-values for the SE(B) specimen with $a/W = 0.5$ predicted from the experimental fracture toughness

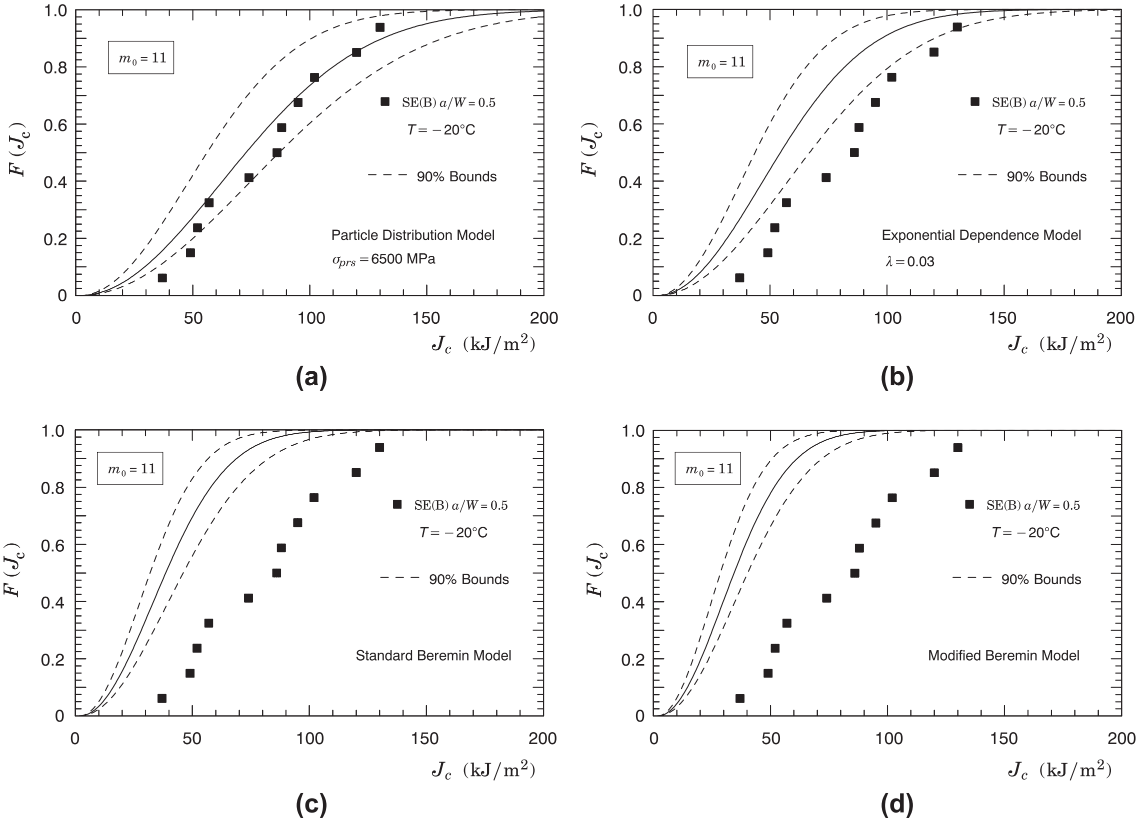

Fig. 15. Predicted cumulative Weibull distribution of experimentally measured J_c-values for the SE(B) specimen with $a/W = 0.5$: (a) Simplified particle distribution model with $\sigma_{prs} = 6500$ MPa and $m_0 = 11$; (b) exponential dependence of eligible microcracks on ϵ_p with $\lambda = 0.03$ and $m_0 = 11$; (c) standard Beremin model; and (d) modified Beremin model.

distribution for the PCVN configuration based on the previous modified Weibull stress models, which include: (1) simplified particle distribution with $\sigma_{prs} = 6500$ MPa; (2) exponential dependence model with $\lambda = 0.03$; (3) standard Beremin model and (4) modified Beremin model. The solid lines in these plots represents the prediction of the median fracture probability whereas the dashed lines define the 90% confidence limits obtained from using the 90% confidence bounds for J_0 determined previously in Section 3.2 – see also Table 2. The predicted Weibull distribution derived from the simplified particle distribution displayed in Fig. 15(a) agrees well with the experimental data; here, most of the measured J_c-values lie within the 90% confidence bounds. In contrast, the predicted Weibull cumulative distribution based on the exponential dependence model, including the 90% confidence bounds, is entirely shifted slightly to the left of the experimental data thereby providing very conservative estimates of fracture toughness for the deeply-cracked SE(B) specimen. Also observe that results for the Beremin model shown in Fig. 15(c) and (d) largely underpredict the experimental distribution of the measured J_c-values.

The relative poor performance of the Beremin model in predicting the J_c-distribution for the deeply-cracked SE(B) specimen also deserves further discussion. As already mentioned, the Weibull modulus, m, has a large effect on the $\tilde{\sigma}_w$-trajectories and, consequently, on determining the relative position of the $\tilde{\sigma}_w$-curves for both specimen geometries. Because of the significant differences in crack front size (and, hence, in the volume of the near-tip fracture process zone – refer to Figs. 8 and 9), the use of larger m-values (other than the initially calibrated Weibull modulus) may help improving the toughness distribution for the deeply-cracked SE(B) geometry. Indeed, conducting the toughness correction $J_0^{PCVN} \rightarrow J_0^{SE(B)-a/W=0.5}$ based on the standard Beremin model with a Weibull modulus of $m = 20$ would yield the predicted characteristic toughness for the deeply-cracked SE(B) specimen as $J_0^{SE(B)-a/W=0.5} = 67$ kJ/m^2, which is now in better agreement, albeit still lower, with the experimental characteristic toughness, $J_0^{SE(B)-a/W=0.5}$. Thus, while using a larger m-value does improve specimen-specific predictions of the J_c-distribution in the present analysis, it is rather of limited use in the present context since the toughness correction $J_{SEB}^{a/W=0.15} \rightarrow J_{SEB}^{a/W=0.5}$ previously described would then not have the correct form. Clearly, there is much to improve on the calibration strategy for the Weibull stress parameters pursued in the present analysis and a followup paper is planned to address this issue.

6.4. Prediction of the reference temperature T_0

Additional analyses to determine the reference temperature, T_0, for the tested material further illustrate the predictive capability of the modified Weibull stress methodology. The procedure essentially repeats the prediction analysis outlined previously in reverse manner. Once a J_0-value for the SE(B) specimen with $a/W = 0.5$ is determined, the reference temperature is obtained by first converting this J_0-value to the corresponding K_0-value and then solving for the median toughness, K_{Jc-med}, as described in Appendix A. The procedure is relatively simple and straightforward while, at the same time, representing well the statistical distribution of measured cleavage fracture toughness data.

Table 4 gives the predicted values of T_0 for all different forms of $\tilde{\sigma}_w$ in connection with varying Ψ_c adopted in the present work. The sensitivity of T_0-predictions on the adopted formulation for $\tilde{\sigma}_w$ becomes clear upon examining these results. In particular, inclusion of plastic strain effects through the modified Weibull stress model based on the simplified particle distribution with $\sigma_{prs} = 6500$ MPa predicts almost exactly the experimental reference temperature for the tested A515 steel given by $T_0 = -41\,^\circ$C derived from the fracture toughness distribution for the deeply-cracked SE(B) specimen tested at $T = -20\,^\circ$C. In contrast, the analyses using other models provide conservative estimates of T_0, ranging from $T_0 = -32\,^\circ$C for the exponential dependence model with $\lambda = 0.03$ to $T_0 = -16\,^\circ$C for the modified Beremin model.

7. Summary and conclusions

This work describes verification studies of a probabilistic framework based on the modified Weibull stress model developed in Part I [11] to predict the effects of constraint loss on macroscopic measures of cleavage fracture toughness applicable to fracture specimens and crack configurations tested in the ductile-to-brittle transition region. The central feature of this methodology lies on the interpretation of the modified Weibull stress, $\tilde{\sigma}_w$, as the probabilistic crack tip driving force coupled with the condition that cleavage fracture occurs when the Weibull stress reaches a critical value, $\tilde{\sigma}_{w,c}$. An important feature of the proposed methodology also includes the effect of near-tip plastic strain on cleavage microcracking which impacts directly the magnitude of $\tilde{\sigma}_{w,c}$ and, consequently, the toughness scaling correction.

A central objective of the present work is to introduce a more advanced and yet simpler methodology for cleavage fracture assessments to describe the fracture process based on local failure criteria coupled with macroscopic (global) fracture parameters, such as the J-integral, thereby removing the specimen geometry and constraint effect dependency of cleavage fracture toughness. Application of the modified Weibull stress methodology predicts accurately well the characteristic toughness, J_0, and the reference temperature, T_0, for an A515 Gr 65 pressure vessel steel tested in the ductile-to-brittle transition region. In particular, T_0-values estimates derived from constraint corrected, small size PCVN specimens are in good agreement with the corresponding estimates derived from testing of much larger crack configurations.

While the correction term included into the modified Weibull stress assumes an *ad hoc* dependence of the fraction of microcracks which are eligible to propagate unstably on the near-tip plastic strain, our exploratory analyses demonstrate the effectiveness and relatively simplicity of the proposed Weibull stress model to provide an engineering approach which unifies toughness measures across different crack configurations and loading modes. However, in interpreting the probabilistic framework presented in this investigation, it is well to keep in mind that a proper choice of the parameters describing plastic strain effects on cleavage fracture (as characterized by the function Ψ_c) introduces another degree of freedom associated with the calibration process thereby adding more complexity to the calibration of the modified Weibull stress parameters.

Our results suggest that a calibration procedure which uses a two-step strategy to identify m and Ψ_c is well suited for analyzing constraint and specimen geometry effects on fracture toughness. We find the method to be consistent with the standard Beremin model as it fully preserves the character of the Weibull modulus, m, as a phenomenological descriptor of the distribution of Griffith-like microcracks that trigger cleavage fracture. Once parameter m is calibrated using the toughness scaling model (TSM) to correct cleavage fracture toughness data measured from two sets of test specimens exhibiting largely contrasting toughness behavior, the process is then repeated to identify the parameters of the function Ψ_c that give the best correction of measured toughness values with the Weibull modulus value now fixed. In particular, our study indicates that the simplified particle distribution (WL) model provides better descriptions of constraint loss and specimen geometry effects as its key parameter, σ_{prs}, plays a stronger role on the $\tilde{\sigma}_w$-trajectories than does parameter λ when using the exponential dependence model.

Overall, the present study provides compelling support for developing fracture assessment methodologies based on $\tilde{\sigma}_w$. However, because of the rather strong sensitivity of the calibrated Weibull modulus, m, on some analysis details, including the toughness ratio J_0^B/J_0^A measured from two sets of test specimens exhibiting largely contrasting toughness behavior used in the TSM procedure, additional work appears necessary to further test the effectiveness of the present framework incorporating various forms of Ψ_c on fracture assessments and toughness predictions for low constraint crack configurations. An investigation along this line is in progress to predict constraint effects on toughness values using subsize fracture specimens for an A533 Gr B steel employed in nuclear reactor pressure vessels [57]. Nevertheless, the analyses conducted in the present work show that the modified Weibull stress approach based on the simplified particle distribution model holds significant promise as an engineering procedure to multiscale predictions of fracture behavior in structural components with diverse range of crack-tip constraint.

Acknowledgments

This investigation is supported by Fundação de Amparo à Pesquisa do Estado de São Paulo (FAPESP) through Grant 2012/13053-2 and by the Brazilian Council for Scientific and Technological Development (CNPq) through Grants 473975/2012-2 and 306193/2013-2. This work was partly conducted while the first author (CR) was on sabbatical at the University of California at Santa Barbara (UCSB). The third author (RHD) was supported by the M.T. Geoffrey Yeh Fund at the University of Illinois at Urbana-Champaign. The authors acknowledge the many useful discussions and contributions of their colleague Prof. George R. Odette (UCSB).

Appendix A. Summary of the master curve approach

Wallin [4–6] has developed a relatively straightforward procedure to characterize fracture toughness data over the DBT region, widely known as the Master Curve approach, which relies on the concept of a normalized curve of median fracture toughness, defined in terms of K_{Jc}-values rather than J_c-values, for 1T ($B = 25$ mm) size specimens vs. temperature applicable to hold experimentally for a wide range of ferritic pressure vessel and structural steels. This section provides a brief overview of the methodology and summarizes the key procedures specified by ASTM E1921 [8]. The approach begins by adopting a three-parameter Weibull distribution [13] to describe the distribution of toughness values in the form

$$F(K_{Jc}) = 1 - \exp\left[-\left(\frac{K_{Jc} - K_{\min}}{K_0 - K_{\min}}\right)^{\alpha}\right] \tag{A.1}$$

in which the Weibull modulus, α, takes the value of 4, $K_{\min}$ defines a threshold fracture toughness (i.e., $F(K_{Jc}) = 0$ for $K_{Jc} \leqslant K_{\min}$) most often assigned a value of 20 MPa $\sqrt{\text{m}}$ and parameter K_{Jc} derives from J_c using the standard relationship

$$K_{Jc} = \sqrt{\frac{EJ_c}{(1 - \nu^2)}}. \tag{A.2}$$

where it is understood that plane-strain conditions are assumed. K_{Jc}-values exceeding $K_{Jc-max} = \sqrt{Eb_0\sigma_{ys}/M}$, where b_0 denotes the original crack ligament size, are set to the limiting value and marked for subsequent censoring. Here, ASTM E1921 [8] specifies a deformation limit of $M = 30$.

For fracture tests performed on other than 1T specimens, the measured toughness values are corrected to their 1T equivalent values using a simple weakest link statistics expressed by

$$K_{Jc-1\text{T}} = 20 + (K_{Jc-X} - 20)\left(\frac{B_X}{B_{1\text{T}}}\right)^{1/4} \quad \text{MPa}\,\sqrt{\text{m}} \tag{A.3}$$

where $B_{1\text{T}}$ is the 1T specimen size (25 mm) and B_X is the corresponding dimension of the test specimens.

Now, following a standard maximum likelihood estimation procedure [8,13], the scale parameter, K_0, corresponding to the 63.2% cumulative failure probability, is given by

$$K_0 = \left[\sum_{k=1}^{N} \frac{(K_{Jc(k)} - 20)^4}{r_c}\right]^{1/4} + 20 \quad \text{MPa}\sqrt{\text{m}} \tag{A.4}$$

where N denotes the total number of tested specimens and r_c represents the number of valid tests (uncensored data). The median toughness at the tested temperature then follows simply as

$$K_{Jc-med} = 0.9124(K_0 - 20) + 20 \quad \text{MPa}\sqrt{\text{m}}. \tag{A.5}$$

The master curve of median toughness, K_{Jc-med}, for 1T specimens over the transition range for the material has the final form

$$K_{Jc-med} = 30 + 70\exp[0.019(T - T_0)] \quad {}^\circ\text{C}, \quad \text{MPa}\sqrt{\text{m}}, \tag{A.6}$$

where T is the test temperature and T_0 is the reference (indexing) temperature. The above expression for the median toughness applies throughout the lower part of the DBT range prior to the appearance of significant ductile tearing. ASTM E1921 [8] test standard also outlines procedures to construct various tolerance bounds based on the above representation for the toughness distribution.

References

[1] American Petroleum Institute, Fitness-for-service. API RP-579-1/ASME FFS-1; 2007.
[2] British Institution. Guide to methods for assessing the acceptability of flaws in metallic structures. BS 7910; 2013.
[3] EDF Energy Nuclear Generation. Assessment of the integrity of structures containing defects, Tech. Rep. R6 Revision 4, UK; 2009.
[4] Wallin K. Fracture toughness transition curve shape for ferritic structural steels, In: Teoh SHSH, Lee KH, editors. Joint FEFG/IICF international conference on fracture of engineering materials and structures. Singapore; 1991. p. 83–8.
[5] Wallin K. Irradiation damage effects on the fracture toughness transition curve shape for reactor pressure vessel steels. Int J Press Vess Piping 1993;55:61–79.
[6] Wallin K. Master curve analysis of the Euro fracture toughness dataset. Engng Fract Mech 2002;69:451–81.
[7] McCabe DE, M JG, Wallin K. An introduction to the development and use of the master curve method. ASTM Manual Series MNL 27, ASTM International; 2005.
[8] American Society for Testing and Materials. Standard test method for determination of reference temperature, T_0, for ferritic steels in the transition range. ASTM E1921-13a; 2013.
[9] Wallin K, Planman T, Valo M, Rintamaa R. Applicability of miniature size bend specimens to determine the master curve reference temperature T_0. Engng Fract Mech 2001;68:1256–96.
[10] Joyce JA, Tregoning RL. Development of the T_0 reference temperature from precracked Charpy specimens. Engng Fract Mech 2001;68:861–94.
[11] Ruggieri C, Dodds RH. An engineering methodology for constraint corrections of elastic–plastic fracture toughness – part I: a review on probabilistic models and exploration of plastic strain effects. Engng Fract Mech 2015;134:368–90.
[12] Beremin FM. A local criterion for cleavage fracture of a nuclear pressure vessel steel. Metall Mater Trans A 1983;14:2277–87.
[13] Mann NR, Schafer RE, Singpurwalla ND. Methods for statistical analysis of reliability and life data. New York: Jonh Wiley & Sons; 1974.
[14] Mudry F. A local approach to cleavage fracture. Nucl Engng Des 1987;105:65–76.
[15] Pineau A. Development of the local approach to fracture over the past 25 years: theory and applications. Int J Fract 2006;138:139–66.
[16] Gao X, Ruggieri C, Dodds R. Calibration of Weibull stress parameters using fracture toughness data. Int J Fract 1998;92:175–200.
[17] Ruggieri C, Gao X, Dodds RH. Transferability of elastic–plastic fracture toughness using the Weibull stress approach: significance of parameter calibration. Engng Fract Mech 2000;67:101–17.
[18] Gao X, Dodds RH. Constraint effects on the ductile-to-brittle transition temperature of ferritic steels: a Weibull stress model. Int J Fract 2000;102:43–69.
[19] Petti JR, Dodds RH. Coupling of the Weibull stress model and macroscale models to predict cleavage fracture. Engng Fract Mech 2004;71:2079–103.
[20] Petti JR, Dodds RH. Calibration of the Weibull stress scale parameter, σ_u, using the master curve. Engng Fract Mech 2005;72:91–120.
[21] Wasiluk B, Petti JR, Dodds RH. Temperature dependence of Weibull stress parameters: studies using the euro-material. Engng Fract Mech 2006;73:1046–69.
[22] Wallin K, Saario T, Törrönen K. Fracture of brittle particles in a ductile matrix. Int J Fract 1987;32:201–9.
[23] Wallin K, Laukkanen A. New developments of the Wallin, Saario, Törrönen cleavage fracture model. Engng Fract Mech 2008;75:3367–77.
[24] Averbach BL. Micro and macro formation. Int J Fract Mech 1965;1:272–90.
[25] Tetelman AS, McEvily AJ. Fracture of structural materials. New York: John Wiley & Sons; 1967.
[26] Hahn GT. The influence of microstructure on brittle fracture toughness. Metall Trans A 1984;15:947–59.
[27] Bordet SR, Karstensen AD, Knowles DM, Wiesner CS. A new statistical local criterion for cleavage fracture in steel. Part I: model presentation. Engng Fract Mech 2005;72:435–52.
[28] Kendall MG, Stuart A. The advanced theory of statistics. 2nd ed. New York: Hafner; 1967.
[29] Feller W. Introduction to probability theory and its application, vol. I. New York: John Wiley & Sons; 1957.
[30] Brindley BJ. The effect of dynamic strain-aging on the ductile fracture process in mild steel. Acta Metall 1970;18:325–9.
[31] Lindley TC, Oates G, Richards CE. A critical appraisal of carbide cracking mechanism in ferritic/carbide aggregates. Acta Metall 1970;18:1127–36.
[32] Gurland J. Observations on the fracture of cementite particles in a spheroidized 1.05% C steel deformed at room temperature. Acta Metall 1972;20:735–41.
[33] Kroon M, Faleskog J. A probabilistic model for cleavage fracture with a length scale influence of material parameters and constraint. Int J Fract 2002;118:99–118.
[34] Gao X, Zhang G, Srivatsan TS. Prediction of cleavage fracture in ferritic steels: a modified Weibull stress model. Mater Sci Engng A 2005;394:210–9.
[35] Ruggieri C. An engineering methodology to assess effects of weld strength mismatch on cleavage fracture toughness using the Weibull stress approach. Int J Fract 2010;164:231–52.
[36] American Society for Testing and Materials. Standard test methods for tension testing of metallic materials, ASTM E8-11; 2011.
[37] American Society for Testing and Materials. Standard test method for notched bar impact testing of metallic materials, ASTM E23-07; 2007.
[38] EricksonKirk MT, Shaikh A, EricksonKirk MA. Insights and observations arising from curve-fitting the Charpy V-notch and tensile data contained within the United States Light Water reactor surveillance database. In: ASME PVP 2008 pressure vessel and piping division conference. Chicago (IL): American Society of Mechanical Engineers; 2008.

[39] American Society for Testing and Materials. Standard test method for measurement of fracture toughness, ASTM E1820-2011; 2011.
[40] American Society for Testing and Materials. Standard test method for determination of reference temperature, T_0, for ferritic steels in the transition range, ASTM E1921-13a; 2013.
[41] Souza RF, Ruggieri C. Revised η-factors and J-CTOD relationships for SE(B) fracture specimens including 3-D effects and implications for fracture toughness measurements. Mater Perform Characteriz 2015;2(2):34–54 [ASTM International].
[42] Wallin K. The scatter in K_{Ic} results. Engng Fract Mech 1984;19:1085–93.
[43] Minami F, Brückner-Foit A, Munz D, Trolldenier B. Estimation procedure for the Weibull parameters used in the local approach. Int J Fract 1992;54:197–210.
[44] Thoman DR, Bain LJ, Antle CE. Inferences on the parameters of the Weibull distribution. Technometrics 1969;11:445–60.
[45] Nevalainen M, Dodds RH. Numerical investigation of 3-D constraint effects on brittle fracture in SE(B) and C(T) specimens. Int J Fract 1995;74:131–61.
[46] Healy B, Gullerud A, Koppenhoefer K, Roy A, RoyChowdhury S, Petti J, et al. WARP3D: 3-D nonlinear finite element analysis of solids for fracture and fatigue processes, Tech. rep. University of Illinois at Urbana-Champaign; 2014 <http://code.google.com/p/warp3d>.
[47] Moran B, Shih CF. A general treatment of crack tip contour integrals. Int J Fract 1987;35:295–310.
[48] Anderson TL. Fracture mechanics: fundaments and applications. 3rd ed. Boca Raton (FL): CRC Press; 2005.
[49] O'Dowd N, Shih C. Family of crack-tip fields characterized by a triaxiality parameter: part I – structure of fields. J Mech Phys Solids 1991;39:989–1015.
[50] O'Dowd N, Shih C. Family of crack-tip fields characterized by a triaxiality parameter: part II – fracture applications. J Mech Phys Solids 1992;40:939–63.
[51] Dodds RH, Shih C, Anderson T. Continuum and micro-mechanics treatment of constraint in fracture. Int J Fract 1993;64:101–33.
[52] Gao X, Dodds RH, Tregoning RL, Joyce JA, Link LR. A Weibull stress model to predict cleavage fracture in plates containing surface cracks. Fat Fract Engng Mater Struct 1999;22:481–93.
[53] Ruggieri C, Dodds RH. A transferability model for brittle fracture including constraint and ductile tearing effects: a probabilistic approach. Int J Fract 1996;79:309–40.
[54] Ruggieri C. WSTRESS Release 3.0: numerical evaluation of probabilistic fracture parameters for 3-D cracked solids and calibration of Weibull stress parameters. Tech. rep., University of São Paulo; 2013.
[55] Ruggieri C. Influence of threshold parameters on cleavage fracture predictions using the Weibull stress model. Int J Fract 2001;110:281–304.
[56] Ruggieri C, Dodds RH. A Weibull stress approach incorporating the coupling effect of constraint and plastic strain in cleavage fracture toughness predictions. In: ASME 2014 pressure vessels & piping conference (PVP 2014). Anaheim (CA); 2014.
[57] Rathbun HJ, Odette GR, Yamamoto T, Lucas GE. Influence of statistical and constraint loss size effects on cleavage fracture toughness in the transition – a single variable experiment and database. Engng Fract Mech 2006;73:134–58.